Doctoral Dissertation

Synthesis and Characterization of Topological Insulators and Related Materials

（トポロジカル絶縁体およびその関連物質の合成と物性研究）

Kazuma Eto

January 2013

Division of Applied Chemistry
Graduate School of Engineering
Osaka University

Preface

The studies presented in this thesis were carried out under the supervision of Professor Yoichi Ando at the Institute of Scientific and Industrial Research, Osaka University.

The objective of this work was to understand Topological Insulators (TIs) characterized by a nontrivial topology of the Hilbert space, which have recently emerged as a new class of quantum materials in solid state physics. There are many opportunities and challenges for the experimental research in this field which can potentially develop useful applications of TIs. In this work, I studied the transport properties of TIs and related materials, and also tried to discover new TI materials.

I hope that the findings and knowledge obtained in my studies would contribute to the progress of fundamental science and practical applications in this field.

Kazuma Eto

Department of Quantum Functional Materials
The Institute of Scientific and Industrial Research
Osaka University
8-1 Mihogaoka, Ibaraki, Osaka 567-0047, Japan

January 2013

List of Contents

Chapter 1 General Introduction

1.1 Topological Insulators and Their Investigations

Recently, a couple of new phenomena called “spin Hall effect” and “quantum spin Hall effect” (Fig.1-1) have attracted considerable attentions, from both theoretical and experimental viewpoint. These effects have an ability to generate spin currents without external magnetic fields due to intrinsic properties of the material. This provides a new pathway to control the spin of electrons, which would be useful in future technologies, in particular, in spintronics.

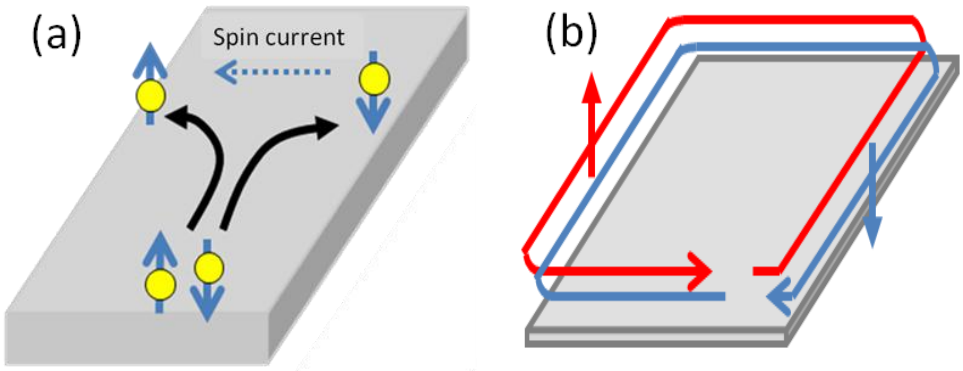

Fig. 1-1. Schematic illustration of (a) spin Hall effect and (b) quantum spin Hall effect.

The spin Hall effect is a transport phenomenon in which an electron spin current is generated in the direction perpendicular to both the applied electric field and the spin polarization axis due to the spin-orbit interaction. This effect appears without breaking the time-reversal symmetry, namely, without applying a magnetic field. The spin Hall effect was first predicted theoretically in 1971 based on an “extrinsic mechanism”, in which impurities in a conducting material deflect the spin-up and spin-down electrons in opposite directions via the so-called skew scattering mechanism [1]. In the early 2000s, the possibility of an “intrinsic mechanism” was also proposed. In this mechanism, a spin current arises from an effective spin-orbit field inherent to the band structure of the material [2,3]. The spin current in the “intrinsic mechanism” is dissipationless, although the charge current is dissipative. The existence of the spin Hall effect was experimentally confirmed in semiconductors and metals [4,5].

The following interesting question was whether the spin Hall effect can be observed in an insulator where the charge current is negligible. Murakami *et al.* proposed that certain band insulators could exhibit intrinsic spin-Hall conductivity without any charge conductivity [6]. However, it has been difficult to distinguish between a "spin Hall insulator" and an ordinary insulator without realizing that there is a topological difference in their ground states [7]. In 2005, Kane and Mele proposed a quantum spin Hall system [8,9] which has an insulating bulk and a gapless metallic edge that carries a spin current.. Such a system can be classified by Z_2 topological numbers [8,10,11], making the quantum spin Hall system to be a 2D topological insulator.

Bernevig, Hughes, and Zhang proposed that CdTe/HgTe/CdTe quantum well can be a candidate for the 2D topological insulator [12]. CdTe has a normal band structure with the valence band originated from atomic *p*-orbitals and the conduction band originated from atomic *s*-orbitals. A thin HgTe layer sandwiched between two CdTe layers also shows a normal band structure due to the quantum confinement effect. However, HgTe has intrinsically an inverted band structure with the valence band originated from *s*-orbitals and the conduction band originated from *p*-orbitals. Thus, upon increasing the thickness of HgTe layer in the CdTe/HgTe/CdTe quantum well, the band inversion is expected, leading to a quantum phase transition from ordinary insulating state to a topological one. Indeed, the 2D quantum spin Hall effect in HgTe quantum well was experimentally observed by König *et al.* [13] in 2007. It was found by König *et al.* that in the quantum spin Hall regime, when the chemical potential is tuned into the bulk forbidden gap, a plateau of residual conductance close to $2e^2/h$, which is independent of the sample width, indicating that it is caused by quantized edge states.

The concept of the quantum spin Hall effect can be generalized to three-dimensional (3D) materials. The idea of a 3D topological insulator (TI) was developed in 2007 by Moore and Balents [14], Fu, Mele, and Kane [10] and also by Roy [15]. Soon after this extension of the TI concept to 3D materials, Fu and Kane [11] realized that the Z_2 topological classification can be simplified in material possessing space inversion symmetry, and they predicted that the $Bi_{1-x}Sb_x$ alloy within a certain range of compositions x (i.e., $0.07 \leq x \leq 0.22$) was going to become a 3D TI [11]. In 2008, using angle-resolved photoemission spectroscopy (ARPES), Hsieh *et al.* observed an odd number of surface states on the (111) plane of $Bi_{0.9}Sb_{0.1}$ [16], which can be considered to give evidence for the topological-insulator nature of this

material. Later, spin-resolved ARPES experiments addressed the spin polarization of the surface states in $Bi_{1-x}Sb_x$ [17,18] and the more precise experiment was able to identify the topologically nontrivial one [18], firmly establishing the topological nature of $Bi_{1-x}Sb_x$.

Unfortunately, the surface band structure of the first TI — $Bi_{1-x}Sb_x$ — was rather complicated. In 2009, much simpler band structures were discovered in the second generation of 3D TIs — Bi_2Se_3, Bi_2Te_3, and Sb_2Te_3 — following theoretical predictions [19]. Namely, it was found by ARPES measurements that the cleaved (111) plane of Bi_2Se_3 and Bi_2Te_3 hosts a single Dirac cone centered at the Γ point [20,21]. Furthermore, spin-polarized ARPES measurements in Bi_2Se_3 and Bi_2Te_3 confirmed the peculiar spin polarization of the surface states [22-24]. The key parameter capable of distinguishing 3D topological insulators from other materials is a strong spin-orbit coupling (SOC). In this respect, compounds containing heavy elements, such as Pb, Bi, Tl, I, Br, Te, Se, are prime candidates for a new topological insulator because of their inherently strong SOC.

Another surface sensitive technique, apart from ARPES, which has been very successful in studying TIs is scanning tunneling spectroscopy (STS) [25-27]. In particular, the suppression of the backscattering of surface electrons, which is one of the main characteristics of TIs, has been confirmed by the analysis of standing-wave interference patterns of scattered quasiparticles observed in $Bi_{1-x}Sb_x$ [25] and Bi_2Te_3 [26].

In addition to ARPES and STS, transport experiments have also been important for understanding the macroscopic properties of topological insulators. The ability to measure and control the transport properties of TIs is essential for making them technologically important materials. However, existing topological insulators are actually not true insulators. They are heavily doped due to the presence of naturally-occurring crystalline imperfections such as vacancies and anti-site defects. Because of such unintentional dopings, it turned out that probing the surface state of TIs in transport experiments is a sort of challenge. To date, there are only a few transport experiments in which transport properties of the surface state have been successfully measured. Peng *et al.* reported transport measurements in Bi_2Se_3 nanoribbons [28], where the bulk contribution to the overall conductance was reduced by the reducing the sample size. The main result of Peng *et al.'s* study was the observation of pronounced Aharonov–Bohm oscillations in the magnetoresistance, which the authors attributed to the coherent propagation of 2D electrons around the perimeter of the nanoribbon, although alternative interpretations could not be excluded

because the Aharonov–Bohm oscillations were rather generic to mesoscopic systems [28]. Similar difficulties in distinguishing signatures of 2D electrons on the TI surface state from ubiquitous mesoscopic effects have been reported in the study on universal conductance fluctuations in nonmetallic Ca-doped Bi_2Se_3 crystals by Checkelsky *et al.* [29,30]. The large amplitude of magneto- fingerprints observed in mm-size bulk samples cannot be attributed solely to the surface electrons, although the phenomenon is likely to be related to some 2D transport channels [30]. These two examples demonstrate how difficult it is to probe transport properties that are directly related to the topological surface state.

Another approach, which I adopted in the present research, is a study of angular-dependent quantum oscillations that can carry clear signatures of 2D topological surface states. An example of a successful application of this method to probe the surface states of TIs is the observation of a coexistence of 2D and 3D states in $Bi_{1-x}Sb_x$ [31,32], which is the first generation TI material with a very small bulk gap and complicated surface bands. Angular-dependent magnetoresistivity measurements turned out to be a very powerful tool for elucidating transport properties of topological surface states in $Bi_{1-x}Sb_x$ and, obviously, they are utilizable in studying other topological insulators and related materials.

Apart from the measurement techniques, finding new topological insulators with better properties is also very important. In particular, a large bulk band gap and ability to tune the chemical potential into the gap are crucial for probing the surface states through transport experiments as well as for utilizing the surface states in real applications. At present, there are many theoretical predictions on new topological insulators [33], and only few of them have been experimentally verified. One of such confirmed TIs is the thallium based bismuth selenide $TlBiSe_2$ which has a large band gap [34-36]. This compound presents a quantum phase transition to a non-topological phase when Se is partly substituted with S in the solid solution $TlBi(S_{1-x}Se_x)_2$ [37,38]. Intriguingly, near this quantum phase transition, it was found that the topological surface state acquires a gap at the Dirac point even though the system does not break the time reversal symmetry [38-40]. I have contributed to the study of this $TlBi(S_{1-x}Se_x)_2$ system, but since my role was not major, the $TlBi(S_{1-x}Se_x)_2$ papers are listed as supplementary publications in this dissertation.

1.2 The Present Work

The angular-dependent magnetoresistance of two materials, PbS and Bi_2Se_3 has been experimentally studied in detail and comprehensively analyzed. In addition, the search for new TI materials has been conducted in the Pb-based system, leading to the experimental discoveries of $Pb(Bi_{1-x}Sb_x)_2Te_4$ and $(PbSe)_5[(Bi_2Se_3)_3]_m$ topological insulators.

In Chapter 2, the experiments to elucidate detailed magnetotransport properties of single crystalline PbS are described. PbS is a prime candidate for the spin Hall insulator due to its strong spin orbit coupling. The observed peculiar angular-dependent magnetoresistance is discussed.

In Chapter 3, the experiments to elucidate detailed magnetotransport properties of single crystalline Bi_2Se_3 are described. Bi_2Se_3 is one of the 3D topological insulators with a simple Dirac-cone surface state. The observed angular-dependent oscillations in magnetoresistance are shown to originate from the Landau level quantization of the 3D Fermi surface of Bi_2Se_3.

In Chapter 4, the study on a Pb-based new topological insulator, $Pb(Bi_{1-x}Sb_x)_2Te_4$, in which the chemical potential can be changed by changing its compositions, is described. The transport properties of this system are also discussed.

In Chapter 5, the study on "natural heterostructures" of topological insulators realized in the Pb-based homologous compounds $(PbSe)_5[(Bi_2Se_3)_3]_m$ is described. ARPES measurements of these compounds elucidated the existence of topological surface states on the hetero-interfaces between $(PbSe)_5$ and $[(Bi_2Se_3)_3]_m$.

Chapter 2 Transport Properties of a Candidate Material for the Spin Hall Insulator: PbS

2.1 Introduction

The existence of spin Hall insulators was predicted by Murakami *et al.* in 2004 [6]. In certain insulators, a finite spin current could arise even without any charge current (Fig.1-1). The candidates for spin Hall insulators are materials which have an energy gap caused by the spin-orbit coupling (SOC). One class of such materials is zero-gap semiconductors such as HgTe, HgSe, β-HgS, and α-Sn. Under a uniaxial strain, these materials acquire a band gap without destroying the spin Hall effect. The other class is narrow-gap semiconductors such as PbTe, PbSe, and PbS, which have strong SOC. Although those lead chalcogenides are not topological insulators [11], the SOC plays an important role in these materials, which are worth investigating with the modern understanding. Crystals of lead chalcogenides are known to be conducting rather than insulating; nevertheless, the concentration of charge carriers can be changed in a wide range, especially in PbS [41-43]. Here, the transport properties of low carrier concentration PbS are described.

PbS has a rock-salt crystal structure and has a direct energy gap of about 0.3 eV located at the four equivalent L points of the Brillouin zone [44]. Depending on whether S is excessive or deficient, both p- and n-type PbS can be prepared, and in both cases the Fermi surface (FS) is very nearly spherical [44,45]. This material was well studied in the past for its potential in the infrared applications [44]. More recently, PbS is attracting attention in the photovoltaic community because of the multi-exciton generation [46]. In the present study, the focus is on the magnetoresistance (MR), especially on its angular dependence. Surprisingly, sharp peaks in the angular-dependent MR in high magnetic fields are observed, which is totally unexpected for a three-dimensional material with a small spherical FS. Although the exact mechanism of this anomalous behavior is not clear at the moment, the data points to an important role of the SOC in the quantum transport regime. In addition, the formation of a surface layer with additional conductivity due to skipping orbits (called “static skin effect” [47]) appears to be also playing a role in the observed angular dependence. The unexpected angular-dependent MR points to a hitherto overlooked effect that could become important in the magnetotransport properties of narrow-gap semiconductors with a strong SOC.

2.2 Experimental

High-quality single crystals of PbS were grown by a vapor-transport method from a stoichiometric mixture of 99.998% purity Pb and 99.99% purity S. The mixture was sealed in an evacuated quartz tube and was reacted for 5–10 h at 980 °C. After the reaction, the resulting material was vaporized and transported to the other end of the sealed tube by making a large temperature difference, which worked as a purification stage. The obtained polycrystals were taken out and again sealed in a new evacuated quartz tube for the crystal growth stage: The polycrystal-containing end of the tube was kept at 850 °C and sublimed PbS was transported to the other end kept at 840 °C for one week. The obtained single crystals were annealed in sulfur vapor to tune the type and the density of carriers, during which the crystal temperature and the sulfur vapor pressure were controlled independently. A series of samples with various carrier densities were prepared as shown in Fig. 2-1. In the following, I focus on the measurements of a *p*-type sample with the carrier density n_h of 4.8×10^{17} cm^{-3}, which was obtained by annealing the crystal at 533 °C with the sulfur vapor source kept at 90 °C.

The resistivity ρ_{xx} and the Hall resistivity ρ_{yx} were measured simultaneously by using a standard six-probe method on a thin rectangular sample whose top and bottom surfaces were cleaved (001) planes. The current I was always along the [100] direction. The Shubnikov-de Haas (SdH) oscillations were measured by sweeping the magnetic field B between +14 and −14 T for a series of field directions. Continuous rotations of the sample in constant magnetic fields were used for measuring the angular dependence of the MR, in which the direction of the magnetic field B was either [001]→[010] (transverse geometry) or [001]→[100] (transverse to longitudinal geometry).

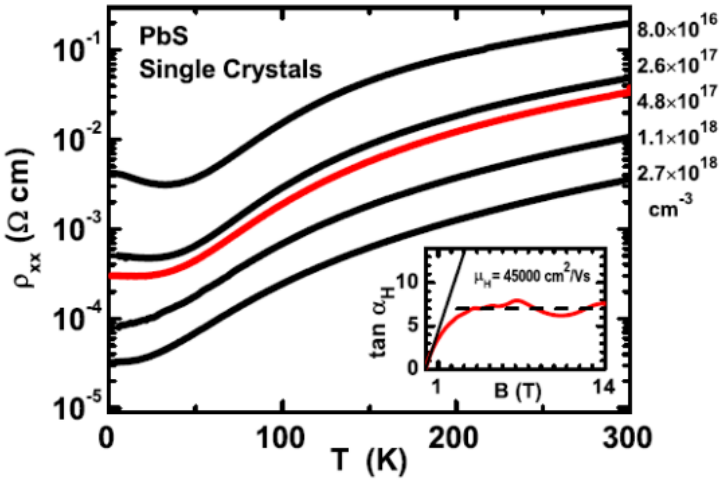

FIG. 2-1. Temperature dependence of ρ_{xx} for a series of p-type PbS single crystals, whose n_h is indicated on the right. Inset shows the tangent of the Hall angle α_H vs B for the 4.8×10^{17} cm^{-3} sample, which exhibits a deviation from the classical linear behavior (shown by the solid straight line) and saturation above 4 T in the quantum transport regime; the low-field slope is equal to μ_H and gives 4.5×10^4 cm^2 /V s.

2.3 Results and Discussion

2.3.1 Magnetoresistance and SdH oscillations

Figure 2-2 shows the transverse MR measured at 1.5 K with B along [001]. Pronounced SdH oscillations are clearly seen and one may notice that the background MR does not show the ordinary B^2 dependence. This is because the range of the weak-field regime ($\mu_H B<1$), where the B^2 dependence is observed, is extremely narrow, as shown in the inset of Fig. 2-2 (μ_H is the Hall mobility). It is worth noting that the sample shows a nearly B-linear background MR in the strong-field regime ($\mu_H B>1$), rather than a tendency to saturation which is usually observed in metals. This high-field behavior is the so-called "quantum linear MR" proposed by Abrikosov [48]. Such behavior is expected in the quantum transport regime where the condition $n_h<(eB/\hbar c)^{2/3}$ is satisfied and in the present sample this regime is realized for $B>4$ T. In this sense, the PbS sample presents a straightforward realization of the quantum linear MR and is different from $Ag_{2+\delta}Se$ or $Ag_{2+\delta}Te$ where the linear MR is observed down to very low field [48].

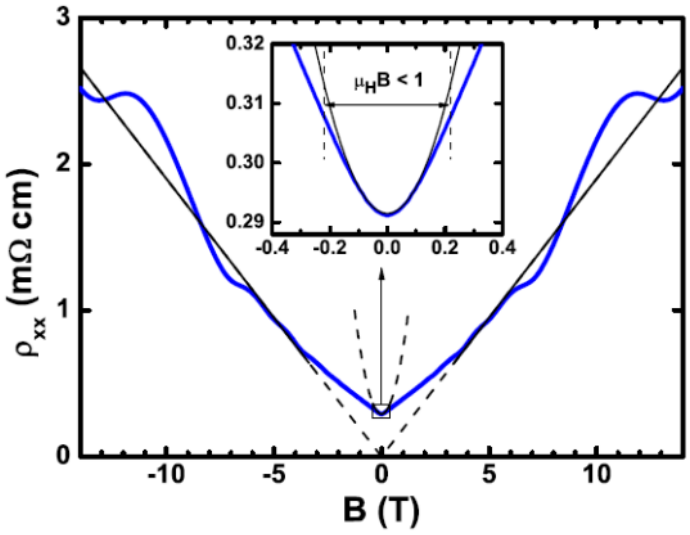

FIG. 2-2. Transverse MR at 1.5 K with B along [001]. The straight lines show the background linear MR, on top of which pronounced SdH oscillations are superimposed. Inset shows the B^2 dependence observed in the low-field classical regime ($\mu_H B<1$) and its fitting (thin solid line).

The SdH oscillations measured in the transverse ($B\perp I$) and longitudinal ($B\parallel I$) MR are presented in Fig. 2-3 by plotting $d\rho_{xx}/dB$ vs $1/B$. One can see the resolved spin splitting of the Landau levels in high magnetic fields and that the crossing of the 0^- state by the Fermi level is observed (the lower left inset of Fig. 2-3 for the Landau-level diagram); this means that all the electrons are in the 0^+ state in the highest field (14 T) and hence the system is in the quantum limit. Also, one may notice that the amplitude of some particular peaks, 0^-, 1^+, and 2^+, are significantly diminished in the longitudinal configuration ($B\parallel I$) compared to the transverse one where all the peaks are well developed. Such behavior was previously observed in $Hg_{1-x}Cd_xTe$ (Ref. 49) and in $Pb_{1-x}Sn_xTe$ (Ref. 50), and was elucidated to be due to some selection rules [49] imposed by the SOC which prohibits scattering between certain Landau sublevels in the longitudinal configuration. Besides this peculiar difference, the peak positions are almost the same for the two field directions, which is because the FS in PbS is nearly spherical [44,45]. Also, the cyclotron mass m_c extracted from the temperature dependence of the SdH amplitude (lower right inset) using the Lifshitz-Kosevich formula [51] is identical for the two directions.

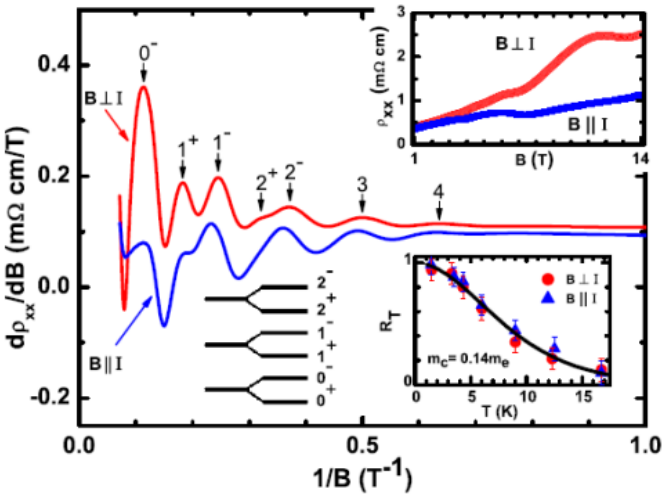

FIG. 2-3. SdH oscillations in the transverse ($B\perp I$) and longitudinal ($B\parallel I$) MR at 1.5 K. Upper inset shows the raw data and the main panel presents $d\rho_{xx}/dB$ vs $1/B$. In the "$B\parallel I$" measurement, the magnetic field was 8° off from the exactly parallel direction. Lower left inset shows the schematic Landau level diagram. Lower right inset shows the temperature dependence of the normalized SdH amplitude, which yields m_c=0.14m_e (m_e is the free electron mass).

The carrier density n_h calculated from the FS volume seen by the SdH oscillations is 4.8×10^{17} cm^{-3}, which agrees well with the value of n_h=4.6×10^{17} cm^{-3} obtained from the high-field Hall coefficient $R_{H\infty}$. It is worth noting that the Hall mobility μ_H calculated from $R_{H\infty}$ and ρ_{xx} at 0 T is 4.5×10^4 cm^2 /V s while the mobility μ_{SdH} obtained from the SdH oscillations is only 3.8×10^3 cm^2 /V s. (Analysis of the SdH data yields T_D=4 K, which gives the scattering time 3×10^{-13} s. Using m_c=0.14m_e, μ_{SdH} =3.8×10^3 cm^2 /V s.) This discrepancy is essentially due to the fact that ρ_{xx} and the Dingle temperature T_D (smearing factor in the SdH effect [51]) are determined by different scattering processes; namely, ρ_{xx} is primarily determined by the backward scattering while T_D is sensitive to both forward and backward scattering [51,52]. Apparently, backward scatterings are much less frequent than the small-angle ones in high-mobility PbS, which leads to the 12 times difference between μ_H and μ_{SdH}.

2.3.2 Angular dependence of magnetoresistance

The angular-dependent MR for the transverse-to-longitudinal rotation (I was along [100] and B was rotated from [001] toward [100]) is shown in Fig. 2-4(a) and the corresponding angular dependence of ρ_{yx} is shown in Fig. 2-4(b) (the magnetic-field angle θ is measured from [001]). In Fig. 2-4(a), pronounced peaks are observed when θ is near 90°, that is, when the magnetic field is slightly inclined from the longitudinal configuration. The θ–dependence of ρ_{yx} also shows a feature near 90°, which can be more easily seen in the upper inset of Fig. 2-4(b) where the deviation of the measured $\rho_{yx}(\theta)$ from a smooth $\cos\theta$ dependence is plotted together with the $\rho_{xx}(\theta)$ data (which is multiplied by 0.3). In this inset, the sharp peak occurs in both ρ_{xx} and ρ_{yx} at the same θ. In addition, $\rho_{yx}(\theta)$ apparently shows periodic oscillations in a wide range of θ, whose relation to the sharp peak is not obvious. In any case, given that the FS in PbS is nearly spherical and that they cannot give rise to any open orbit, such a sharp peak in the angular-dependent MR is totally unexpected.

To gain insight into the origin of the unexpected peak in $\rho_{xx}(\theta)$, the angular-dependent MR data in a different rotation plane is useful. Figure 2-5 shows such data for the transverse rotation (I was along [100] and B was rotated from [001] toward [010]). In Fig. 2-5, there is no sharp peak in this configuration, which indicates that the unexpected peaks are peculiar to the near-longitudinal configuration. Besides the absence of the sharp peaks, there is a notable feature in Fig. 2-5: since PbS has a cubic symmetry, the MR for θ=0° (B along [001]) and 90° (B along [010]) should be the same since [001] and [010] are crystallographically identical and the measurement configuration is both transverse. However, the actual data in Fig. 2-5 indicates that they are different, which suggests that there must be some additional factor which affects the resistivity in magnetic field. In the past, similar anisotropy was observed in clean specimens of low-carrier-density materials such as Bi (Ref. 53) and Sb (Ref. 54), and was explained in terms of the static skin effect [47], that is, the formation of a surface layer of additional conductivity due to skipping orbits when the magnetic field is nearly parallel to a specular surface. In this regard, since the top and bottom surfaces of the sample were cleaved (001) plane, it is understandable that the static skin effect creates a surface conduction layer near the specular (001) surface for the magnetic field along [010], leading to a reduced resistivity.

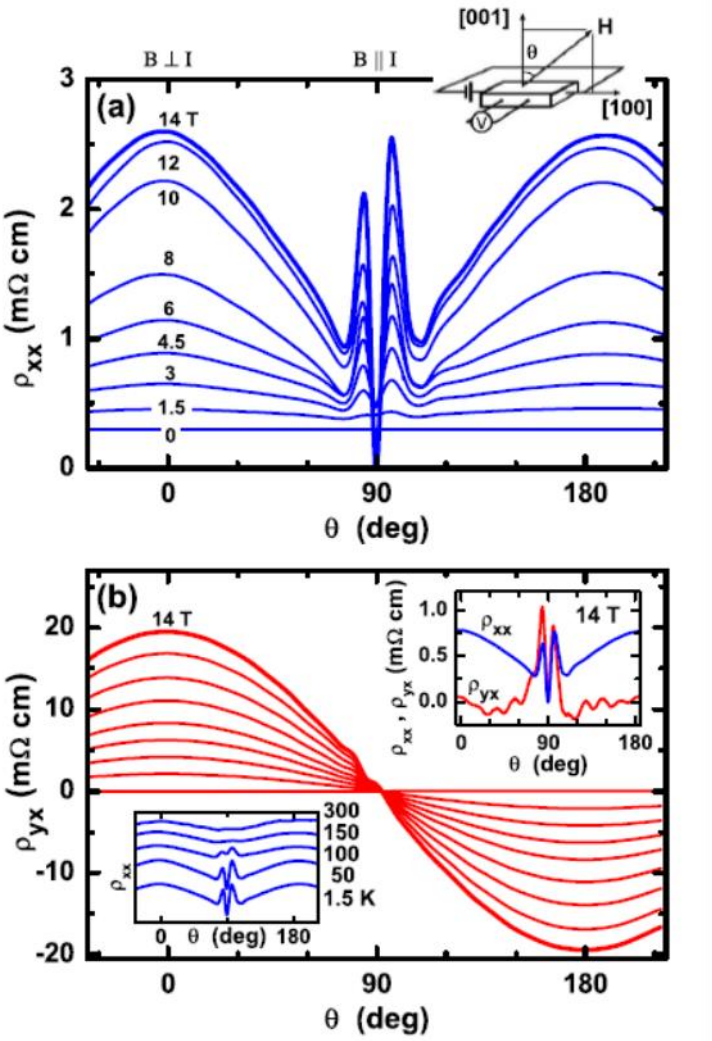

FIG. 2-4. Angular dependence of (a) ρ_{xx} and (b) ρ_{yx} for the transverse-to-longitudinal rotation (top inset shows the geometry). In panel (b), the upper inset compares the deviation of $\rho_{yx}(\theta)$ from the $\cos\theta$ dependence to $\rho_{xx}(\theta)$ multiplied by 0.3 while the lower inset shows how the anomalous peaks weaken with temperature (data are vertically shifted for clarity).

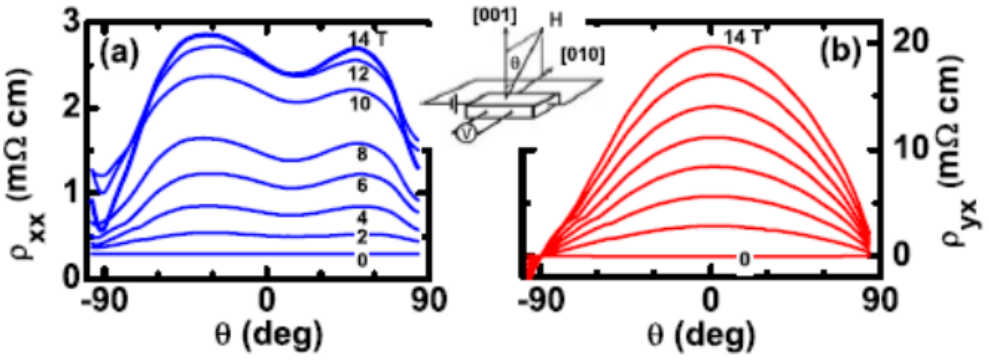

FIG. 2-5. Angular dependence of (a) ρ_{xx} and (b) ρ_{yx} for the transverse rotation (inset shows the geometry). The ρ_{xx} data shown here are after removing the admixture of the ρ_{yx} component in the ρ_{xx} measurement.

An additional factor to consider regarding the MR anisotropy in the present case is the SOC which diminishes some of the peaks in the SdH oscillations for $B \parallel I$. In fact, as one can infer in the upper inset of Fig. 2-3, the change in the SdH oscillations due to the SOC is partly responsible for the difference in MR between $B \perp I$ and $B \parallel I$. Another factor to consider is the crossover between classical and quantum transport regimes: as already discussed, the quantum regime is arrived above 4 T in the transverse configuration. This crossover can also be seen in the B dependence of $\tan\alpha_H$, which is linear in B in the classical regime but saturates in the quantum regime (in the quantum regime, both ρ_{xx} and ρ_{yx} becomes linear in B, leading to a constant $\tan\alpha_H$.), see Fig. 2-1 inset. On the other hand, in the longitudinal configuration, the electron motion along the current direction is *not* quantized and therefore ρ_{xx} for $B \parallel I$ is always "classical." This means that in the measurement in high magnetic fields, there is a crossover from the classical to the quantum regime when the configuration changes from longitudinal to transverse. Since the MR behavior is different in the two regimes, this crossover must be partly responsible for the observed MR anisotropy.

Although the mechanism responsible for the sharp peaks in the angular-dependent MR shown in Fig. 2-4(a) is not clearly established, it can be pointed out that there are three factors that are likely to participate in this phenomenon: (i) the SOC which diminishes some of the peaks in the SdH oscillations for $B \parallel I$, (ii) the static skin effect which creates a conducting surface layer, and (iii) the crossover between classical and quantum transport regimes. It is useful to note that the sharp peaks weaken only gradually with increasing temperature and are still observable at 100 K [lower inset of Fig. 2-4(b)] while the SdH oscillations disappear above ~20 K (lower right inset of Fig. 2-3); this suggests that the sharp peak is not directly related to quantum oscillations. It should also be noted that the SOC is expected to affect not only the SdH oscillations but also the static skin effect when the magnetic field is inclined from the surface because in such configuration the surface reflection of an electrons necessarily involves a transition to a different Landau level [47] and the same selection rules imposed by the SOC as those in the SdH case [49] would apply. Hence, it is expected that the anomalous angular-dependent MR is a result of an intricate interplay between the above three factors.

2.4 Conclusions

The sharp peaks were observed in the angular-dependent MR in PbS when the magnetic field is slightly inclined from the longitudinal ($B \parallel I$) configuration, which is totally unexpected for a low-carrier-density system with nearly spherical Fermi surface. While the mechanism of these peaks is to be elucidated in future, one may conclude that the spin-orbit coupling, the static skin effect, and the crossover between classical and quantum transport regimes, play an important role in the magnetotransport in PbS. The observed unusual phenomenon is helpful for establishing a general understanding of the magnetotransport in narrow-gap semiconductors with a strong SOC, which is important for elucidating transport properties of topological insulators.

Chapter 3 Angular-Dependent Oscillations of the Magnetoresistance in Bi_2Se_3

3.1 Introduction

Bi_2Se_3 is a semiconductor well-known for its thermoelectric properties. It has a rhombohedral crystal structure (space group $D_{3d}^5 - R\bar{3}m$). The unit cell consists of a stack of three quintuple layers, where each quintuple layer consists of a Se(1)–Bi–Se(2)–Bi–Se(1) sequence along the c-axis. Although the bulk of the material has a band gap of moderate size (0.3 eV), its charge transport properties can vary significantly depending on sample preparation conditions [55], showing a strong tendency to be *n*-type due to Se vacancies for Bi-rich/Se-poor conditions or antisite defects with Se in the Bi site for Bi-poor/Se-rich conditions. As mentioned in Chapter 1, Bi_2Se_3 is a topological insulator with a single surface Dirac cone [20] and, for this reason, it is the most studied topological insulator so far.

As also mentioned in Chapter 1, capturing a signature of the surface state of a topological insulator in its transport properties is a challenge, mostly because of dominating bulk conductivity in real TI materials. In this respect, the angular-dependent MR is a powerful tool for distinguishing contributions to the transport properties from coexisting 3D and 2D Fermi surfaces in TIs, as will be shown in this chapter. The pronounced angular-dependent oscillations in the MR, which are observed in an *n*-type Bi_2Se_3 single crystal with the carrier density n_e=5×10^{18} cm^{-3}, are shown to be essentially due to the Landau level quantization of the anisotropic bulk FS of this material, providing a useful reference for discriminating the contributions of 2D and 3D FSs in the magnetoresistance of Bi_2Se_3.

3.2 Experimental

High-quality Bi_2Se_3 single crystals were grown by melting stoichiometric mixtures of 99.9999% purity Bi and 99.999% purity Se elements in sealed evacuated quartz tubes. After slowly cooling from the melting point down to about 550°C over two days, crystals were kept at this temperature for several days and then were furnace cooled to room temperature. The obtained crystals are easily cleaved and reveal a flat shiny surface. The x-ray diffraction measurements confirmed the rhombohedral crystal structure of Bi_2Se_3. A postgrowth annealing at 550°C under controlled selenium partial pressure was used to reduce the number of selenium vacancies that are responsible for creating electron carriers [30].

The resistivity ρ_{xx} was measured with a standard four-probe method on rectangular samples with the electric current I directed along the C_1 axis. Continuous rotations of the sample in constant magnetic field B were used to measure the angular dependence of the transverse MR within the C_3-C_2 plane. For some selected magnetic field directions, the field dependences of ρ_{xx} and the Hall resistivity ρ_{yx} were also measured by sweeping B between ±14 T.

3.3 Results and Discussion

3.3.1 Resistivity and SdH oscillations

Figure 3-1 shows the temperature dependence of ρ_{xx} of the Bi_2Se_3 single crystal studied in this work. It shows a metallic behavior $d\rho/dT>0$ down to ~30 K, and saturates at lower temperature (there is actually a weak minimum near 30 K, as is usually observed [56,57] in low-carrier-density Bi_2Se_3). The single-crystal nature of the sample is evident in the x-ray diffraction data shown in the upper inset of Fig. 3-1. The lower inset of Fig. 3-1 shows the Hall resistivity ρ_{yx} measured at 1.5 K for the field direction along the C_3 axis, which suggests that the main carriers are electrons and the carrier density n_e is 3.4×10^{18} cm^{-3} (in a one-band model). From the values of the Hall coefficient R_H=1.82 cm^3 /C and ρ_{xx}=0.28 mΩ cm at 1.5 K, the Hall mobility μ_H is estimated to be 6500 cm^2 /V s.

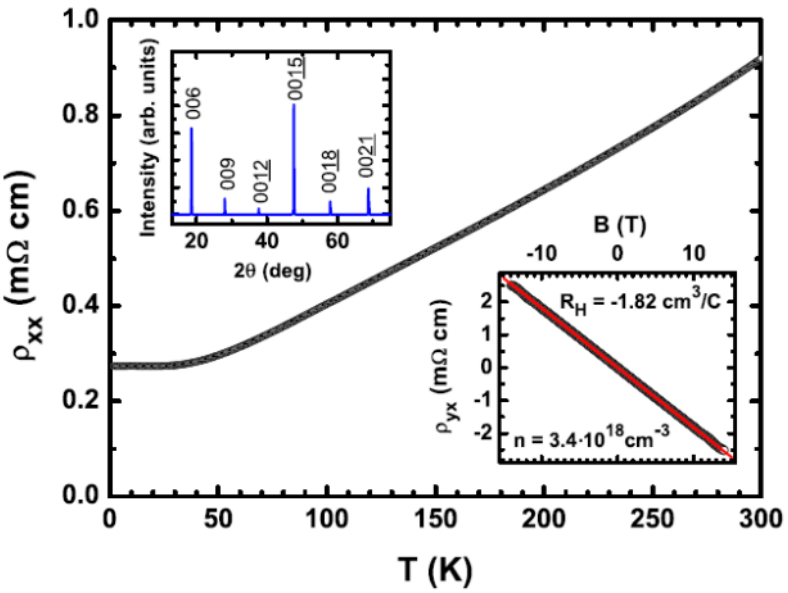

FIG. 3-1. Temperature dependence of ρ_{xx} in 0 T. Upper inset shows the x-ray diffraction pattern of the Bi_2Se_3 single crystal used for transport measurements. Lower inset shows ρ_{yx} for $B \parallel C_3$ measured at 1.5 K. The slope of $\rho_{yx}(B)$, shown by the thin solid line, suggests that the main carriers are electrons whose density is 3.4×10^{18} cm^{-3}.

Figure 3-2 shows $\rho_{xx}(B)$ measured at 1.5 K for several field directions in the transverse geometry ($I \parallel C_1$ and $B \perp I$), after removing the antisymmetric components due to the admixture of ρ_{yx}. Two features are evident: first, pronounced SdH oscillations are seen for any field direction, suggesting their 3D origin. Second, the background of the SdH oscillations varies significantly with the field direction, indicating that the transverse MR is very anisotropic. Both features are taken into account in the simulation of the observed angular dependence of the MR, as will be discussed below.

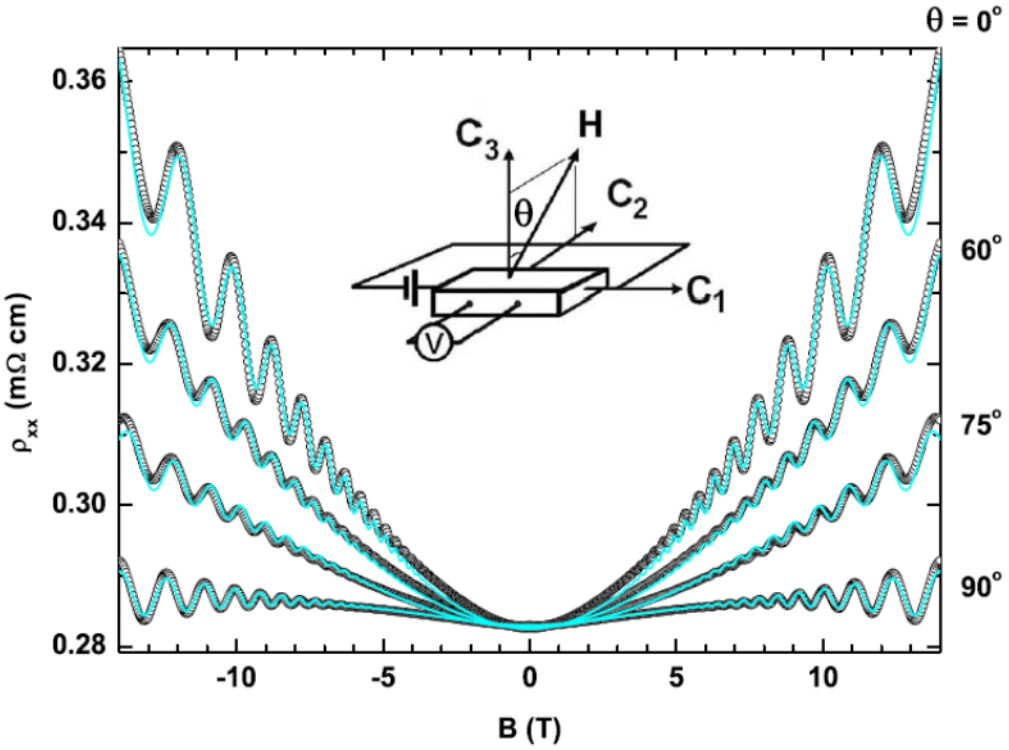

FIG. 3-2. SdH oscillations measured within the C_3-C_2 plane. Thin solid lines are the result of $\rho_{xx}(B)$ simulation using Eq. (1). Inset shows the measurement configuration.

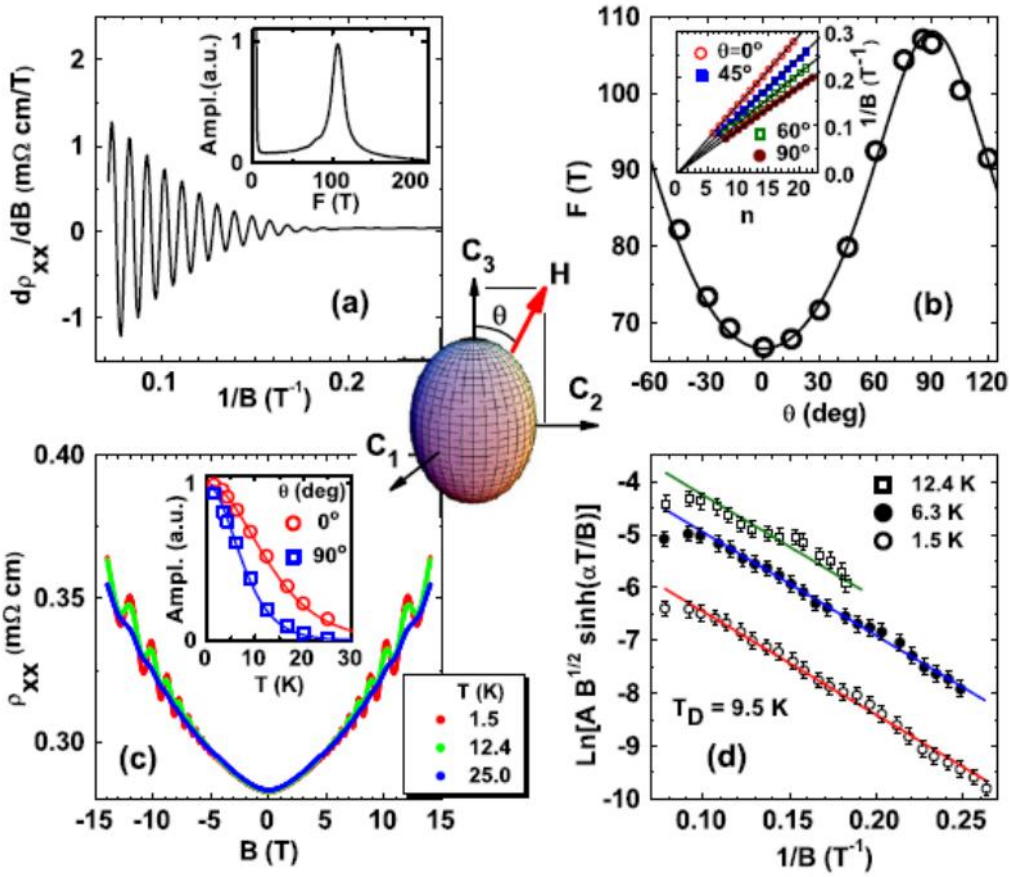

FIG. 3-3. Analyses of the SdH oscillations. The inset in the middle schematically shows the obtained 3D Fermi surface and the definition of θ. (a) SdH oscillations for $B \parallel C_2$ as a function of $1/B$. The Fourier transform shown in the inset reveals a single frequency $F =$ 107 T. (b) $F(\theta)$ measured within the C_3-C_2 plane; inset shows the fan diagram for several θ. (c) Temperature dependence of the SdH oscillations for $B \parallel C_3$; inset shows the temperature dependences of the SdH amplitudes measured along the C_3 and C_2 axes at 12 T, yielding the cyclotron mass of $0.14m_e$ and $0.24m_e$, respectively. (d) Dingle plots for $B \parallel C_3$ at several temperatures give the same $T_D =$ 9.5 K.

Figure 3-3 presents the analysis of the observed SdH oscillations. The oscillations in $d\rho_{xx}/dB$ plotted as a function of $1/B$ for $B \parallel C_2$ (θ=90°) are shown in Fig. 3-3(a) as an example. The very simple pattern seen in Fig. 3-3(a) is a result of the single frequency F=107 T (see inset for the Fourier transform) governing the SdH oscillations. The same analysis was applied to the data for other field directions, and the obtained F as a function of θ is shown in Fig. 3-3(b). The same set of frequencies can be extracted from the Landau-level "fan diagram" [inset of Fig. 3-3(b)], which is a plot of the positions of maxima in $\rho_{xx}(B)$ as a function of the Landau-level numbers. The slopes of the straight lines in the fan diagram give exactly the same $F(\theta)$ as the Fourier transform result. Another piece of information that can be extracted from the fan diagram is the phase of the oscillations, γ, which is determined by $\rho_{xx} \sim \cos[2\pi(F/B+\gamma)]$. In the present case, all the straight lines in the inset of Fig. 3-3(b) intersect the horizontal axis at the same point, giving γ=0.4 that is independent of the field direction. The angular dependence of the SdH frequency $F(\theta)$ points to a single ellipsoidal FS located at the Γ point with the semiaxes $k_a = k_b = 4.5\times10^6$ cm^{-1} ($\perp C_3$) and $k_c = 7.3\times10^6$ cm^{-1} ($\parallel C_3$). The expected $F(\theta)$ for this FS is shown by the solid line in Fig. 3-3(b), which fits the data very well. The carrier density corresponding to this FS is 5×10^{18} cm^{-3}, which is about 50% higher than that obtained from R_H, as was reported previously in the literature [58]. This discrepancy is due, at least partly, to the fact that the present R_H was measured in the low-field limit and contains the so-called Hall factor, which is usually between 1–2.

The temperature dependence of the SdH oscillations was measured for two field directions, along the C_3 and C_2 axes. Figure 3-3(c) shows the $\rho_{xx}(B)$ data in $B \parallel C_3$ for some selected temperatures, where one can see that the background MR is essentially temperature independent and that oscillations are still visible even at 25 K. The inset of Fig. 3-3(c) shows the temperature dependence of the SdH amplitude measured at 12 T for B along C_3 (θ=0°) and C_2 (θ =90°). The fits with the standard Lifshitz-Kosevich theory [51] yield the cyclotron mass m_c of $0.14m_e$ and $0.24m_e$ for θ =0° and 90°, respectively. The energy dispersion near the conduction-band minimum of Bi_2Se_3 is known to be parabolic [58], and the observed anisotropy in m_c for the given FS is entirely consistent with the parabolic dispersion to within 5%. Relying on this dispersion, the Fermi energy E_F is calculated to be 56 meV and the Fermi velocity v_F is 3.8×10^7 cm/ s for any direction.

The Dingle plots [shown in Fig. 3-3(d) for $B /\!/ C_3$ as an example] yield the Dingle temperature T_D=9.5 K which is almost isotropic and is constant at low temperature; this gives an isotropic scattering time τ=1.3×10^{-13} s, implying the mean free path ℓ (=$v_F\tau$) of ~50 nm and the mobility μ_{SdH} of about 1600 cm^2/V s, which is almost four times smaller than μ_H estimated from R_H. Such discrepancy between μ_{SdH} and μ_H has long been noted in various systems [51], and the essential reason lies in the difference in how the effective scattering time comes about from the microscopic scattering process [52]. The scattering rate $1/\tau_{tr}$ determining transport properties acquires the additional factor $1-\cos\phi$ upon spatial averaging (ϕ is the scattering angle), while $1/\tau$ to govern the dephasing in the quantum oscillations is given by a simple spatial averaging without such a factor. Hence, if the small-angle scattering becomes dominant (which is often the case at low temperature), $1/\tau_{tr}$ can be much smaller than $1/\tau$. This means that the mean free path in the sample can be even larger than that estimated above.

3.3.2 Angular-dependent MR oscillations

It is interesting to note that the oscillatory angular dependence of the MR shown in Fig. 3-4(a), where, on top of the twofold-symmetric background angular dependence, pronounced oscillations are evident at higher fields. These oscillations differ from the celebrated angular-dependent magnetoresistance oscillations (AMRO) thoroughly studied in low-dimensional quasi-1D and quasi-2D organic compounds in the last two decades [59-65]. The salient feature of the ordinary AMRO is that oscillations are periodic in $\tan\theta$, where θ is the angle between the applied field and the axis normal to a conducting plane (or chain, in the case of quasi-1D materials). Consequently, the positions of AMRO peaks are independent of the magnetic field in contrast to the data shown in Fig. 3-4(a). The origin of the AMRO is now well understood and, generally, it can be regarded as a result of interlayer (or interchain) tunneling of charge carriers in low-dimensional materials [63-65]. In the data shown in Fig. 3-4(a), the peak positions shift with magnetic field, which is not expected if it were due to the ordinary AMRO. In the following, those oscillations in Bi_2Se_3 are shown to be due to the Landau quantization of the 3D FS and, hence, are essentially of the same origin as the SdH oscillations. The SdH oscillations occur as the Landau-quantized cylinders in the Brillouin zone expand and cross the FS with increasing magnetic field, while the angular-dependent oscillations occur as the axis of those cylinders rotates in the Brillouin zone.

Obviously, no oscillation is expected for rotating magnetic field when the FS is spherical, but when the FS is anisotropic, the number of cylinders residing within the FS changes as the cylinder axis is rotated, leading to resistivity oscillations. Therefore, an anisotropy in the FS is a necessary ingredient for the angular-dependent oscillations.

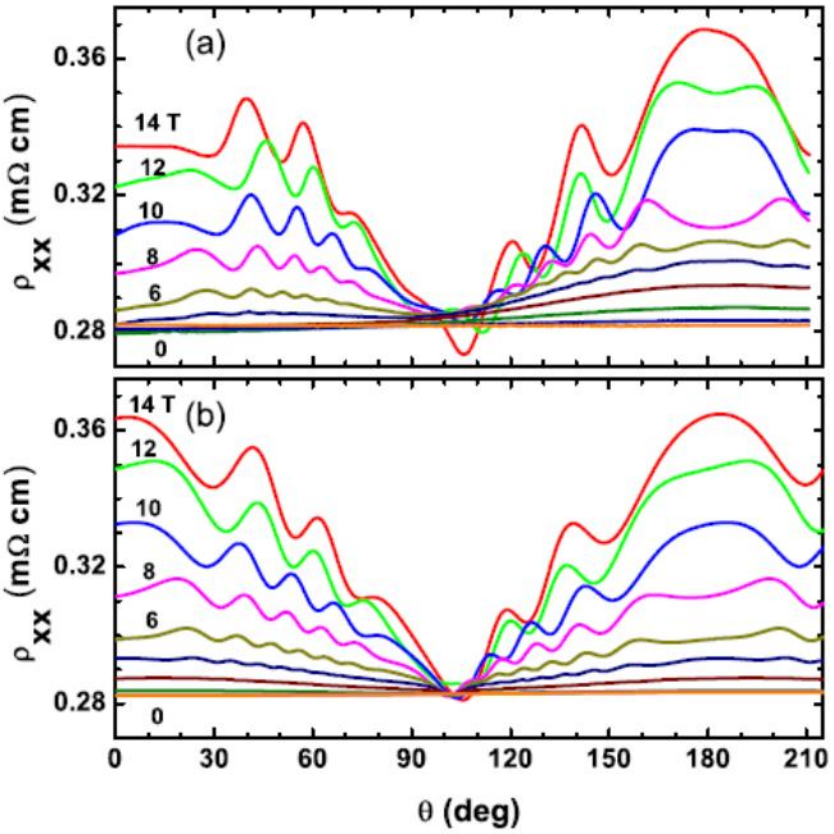

FIG. 3-4. (a) Angular dependences of ρ_{xx} at 1.5 K measured within the C_3-C_2 plane in constant magnetic fields, whose values were 0, 0.5, 1.5, 3, 4.5, 6, 8, 10, 12, and 14 T. (b) Simulation of ρ_{xx} based on Eq. (1) for the same magnetic fields as in (a).

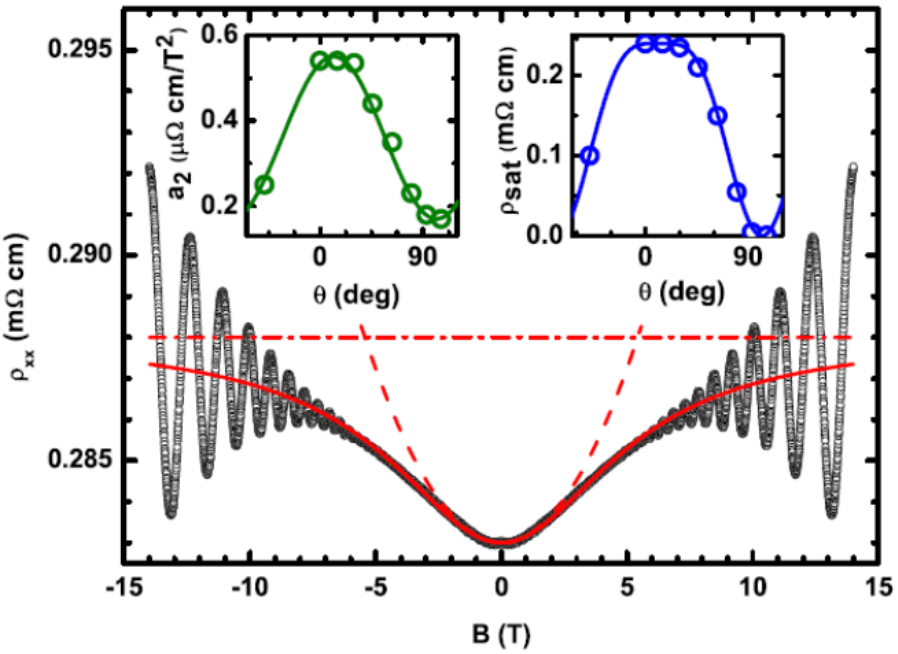

FIG. 3-5. Fitting of the background MR for $B \parallel C_2$. Open circles show the experimental data [symmetrical component of $\rho_{xx}(B)$]; the dashed line demonstrates the low-field quadratic dependence of the resistivity, $\rho_{qd}(B) = a_2 B^2$; the dashed-dotted line represents the high-field saturation limit, ρ_{sat}; the solid line is the resulting reconstructed background, $\rho_{BG}(B)$ which can be described as $1/\rho_{BG} = 1/\rho_{qd}+1/\rho_{sat}$. The left and right insets show the obtained angular dependences of the coefficients a_2 and ρ_{sat} within the C_3-C_2 plane.

To show that the observed angular-dependent oscillations are essentially due to the Landau quantization, it would be most convincing to reconstruct the angular dependence of the MR based on the observed data of SdH oscillations. For this purpose, one needs to understand the exact magnetic field dependence of the MR in the presence of the SdH effect, and know how it evolves when the magnetic field is rotated. Figure 3-5 shows the $\rho_{xx}(B)$ data for $B \parallel C_2$ (θ=90°), which is an example for presenting the procedure to extract the necessary information. At low magnetic fields, the MR in Fig. 3-5 exhibits an almost quadratic field dependence, which can be fitted by $\rho_{qd}(B)=a_2B^2$. With increasing magnetic field, the MR tends to saturate, while pronounced SdH oscillations develop at the same time. The overall background MR $\rho_{BG}(B)$ can be described as $1/\rho_{BG} = 1/\rho_{qd}+1/\rho_{sat}$, which combines the low-field quadratic behavior and the high-field saturation of $\rho_{xx}(B)$. This background develops on top of the zero-field resistivity $\rho_{xx}(0)$ of about 0.28 mΩ cm. The same fitting of the background of MR can be made for the whole range of the magnetic field direction. The evolutions of the parameters a_2 and ρ_{sat} with θ in the C_3-C_2 plane are shown in the left and right insets of Fig. 3-5. The significant difference in the magnetoresistance background measured along the C_3 and C_2 axes is presumably related to the in-plane/out-of-plane MR anisotropy reflecting the crystal symmetry. Note that the center of the symmetry for both $a_2(\theta)$ and $\rho_{sat}(\theta)$ is shifted from θ=0° by about 12°, which is probably due to the rhombohedral symmetry of the crystal which leads to the appearance of cross terms [66] in the magnetic field expansion of the resistivity tensor. This shift causes a pronounced asymmetry in the angular dependence of ρ_{xx} (Fig. 3-4) but is not responsible for the shift of the peaks in the angular oscillations with the magnetic field.

Once ρ_{BG} is known as functions of both θ and B, one can superpose the SdH oscillations to obtain the expected $\rho_{xx}(\theta, B)$. In the case of the Bi_2Se_3 sample, thanks to the fact that the SdH oscillations are composed of only one frequency, one can simulate experimental data as

$$\rho_{xx}(\theta, B) = \rho_{BG}(\theta, B)\left(1 + AR_T R_D \cos\left[2\pi\left(\frac{F(\theta)}{B} + \gamma\right)\right]\right), \qquad (1)$$

where $R_T = 2\pi^2(k_B T/\hbar\omega_c)/\sinh[2\pi^2(k_B T/\hbar\omega_c)]$ and $R_D = \exp[-2\pi^2(k_B T_D/\hbar\omega_c)]$ are temperature and Dingle damping factors, respectively [51]. F is the frequency and γ is the phase of the SdH oscillations. k_B is Boltzmann constant, $\hbar$ is reduced Plank constant, T is temperature, ω_c is cyclotron frequency, and T_D is Dingle temperature. Note that, because only a single frequency is observed in the Fourier transform spectrum and no sign of spin splitting of energy levels was found, here it is assumed that the spin-damping factor R_S to be equal to one. The actual value of R_S does not affect the angular dependence of ρ_{xx} and can only change the coefficient A. As shown in Fig. 3-2 by thin solid lines, the experimentally observed SdH oscillations are reproduced reasonably well with Eq. (1) with a parameter $A = 0.12$ which is independent of θ, B, and T.

The same set of parameters can be used to calculate $\rho_{xx}(\theta)$, namely, the angular-dependent MR for fixed B, with Eq. (1). The result is shown in Fig. 3-4(b), where one can easily see that the calculated angular dependences of the MR follow very closely the rather complicated patterns of the observed $\rho_{xx}(\theta)$. This gives compelling evidence that the angular-dependent oscillations are essentially due to the Landau quantization of the anisotropic 3D FS.

It was emphasized in Ref. 32 that a merit of measuring the angular dependence of the MR is that at sufficiently high magnetic field, the 3D FS remains in the quantum limit (where all the electrons condense into the first Landau level) and does not contribute to the angular-dependent oscillations, while the 2D FS will always produce MR oscillations when the magnetic field direction is nearly parallel to the 2D plane. Once the density of the residual carriers in a topological insulator sample is sufficiently reduced, the 3D FS should be easily brought into the quantum limit and the 2D FS would become distinguishable in the angular-dependent MR oscillations. Also, the SdH effect needs a certain range of magnetic field for the oscillations to be recognized, whereas the observation of the angular-dependent oscillations can be made only at the highest field; this gives a certain practical advantage

to the latter method when the quantization condition is only barely achieved with the available magnetic field. Therefore, one would expect that the angular dependence of the MR will be a useful tool for distinguishing the 2D surface state of the topological insulator Bi_2Se_3 when a single crystal with much lower carrier density becomes available.

3.4 Conclusions

In conclusion, pronounced angular-dependent oscillations of the MR have been observed in high-quality single crystals of *n*-type Bi_2Se_3 with $n_e = 5\times10^{18}$ cm^{-3}. By simulating the angular-dependent oscillations based on the information obtained from the SdH analysis, it was concluded that the oscillations are essentially due to the Landau quantization of the 3D bulk Fermi surface. This provides a compelling demonstration of how the Landau quantization of a closed 3D FS can give rise to pronounced angular-dependent MR oscillations. Furthermore, the present results pave the way for distinguishing the 2D surface state in Bi_2Se_3 in future studies of the angular-dependent MR, by completely elucidating the oscillations due to the bulk FS.

Chapter 4 Pb-Based New Topological Insulator $Pb(Bi_{1-x}Sb_x)_2Te_4$

4.1 Introduction

The discovery of the Bi_2Se_3 family of TIs [19,20] inspired a search for new topological materials. Pb- and Tl-based chalcogenides, which bear some similarities to the Bi_2Se_3 family, have immediately attracted attention due to the strong SOC of the elements they contain. The thallium (Tl)-based chalcogenides $TlBiX_2$ and $TlSbX_2$ (X = Te, Se, S) were predicted [67-69] to be 3D TIs, what was soon confirmed experimentally [34-36]. These compounds have a rhombohedral crystal structure (D_{3d}^5–$R\bar{3}m$) similar to Bi_2Se_3.

Similarly, on the basis of the band structure calculations, it was proposed [70-72] that lead (Pb)-based layered ternary chalcogenides PbM_2X_4 (M = Bi, Sb; X = Se, Te) are promising candidates of 3D TIs. According to the calculations, some compounds in this system show a single Dirac cone at the center of the surface Brillouin zone, and a band inversion takes place at the Z or Γ point in the bulk Brillouin zone [71,72]. However, in 2011 when the present experiment was conducted, there was no clear experimental demonstration of the TI nature in Pb-based ternary chalcogenides. A potential advantage of the PbM_2X_4 system, which makes it very attractive for transport experiments, is a possibility to change the concentration and the type of charge carriers by partially substituting Bi for Sb in the M-site.

The study shown in this chapter has been done by focusing on the Pb-based solid solution $Pb(Bi_{1-x}Sb_x)_2Te_4$. The Bi-end of this solid solution, $PbBi_2Te_4$ (x=0), is an electron-doped compound, while the Sb-end, $PbSb_2Te_4$ (x=1), is a hole-doped one. Both have a tetradymite-like layered structure with space group $R\bar{3}m$. Naturally, it is expected that the carrier concentration will change gradually form n-type to p-type in the solid solution and, therefore, can be adjustable as a function of x. The two end members of PbM_2Te_4 were studied in some detail in the past with the main focus on their thermoelectric properties [73-74], but not much was known about their solid-solutions. $Pb(Bi_{1-x}Sb_x)_2Te_4$ has a rhombohedral crystal structure with the layers stacked along the [111] direction as shown in Fig. 4-1(a). It consists of septuple layers where Pb atoms are sandwiched by Te-(Bi/Sb)-Te layers, with a space inversion symmetry centered at the Pb atom. The crystals cleave between two septuple layers which are weakly coupled by van der Waals interactions. The bulk Brillouin zone and its projected surface Brillouin zone onto the (111) plane are shown in Fig. 4-1(b). Note that the bulk Brillouin zone is shrunk along the [111] direction by ~30%

with respect to that of the prototypical topological insulator Bi_2Te_3 owing to the longer *c* axis.

In the following, angle-resolved photoemission spectroscopy measurements and transport measurements of Pb-based ternary chalcogenides $Pb(Bi_{1-x}Sb_x)_2Te_4$ are described. By observing a single Dirac-cone surface band structure at the Brillouin-zone center, it was experimentally demonstrated that this system constitutes a new family of 3D topological insulators. It was also confirmed that the chemical potential μ (and thus the sign of the Dirac carriers) is tunable by controlling the Bi/Sb ratio.

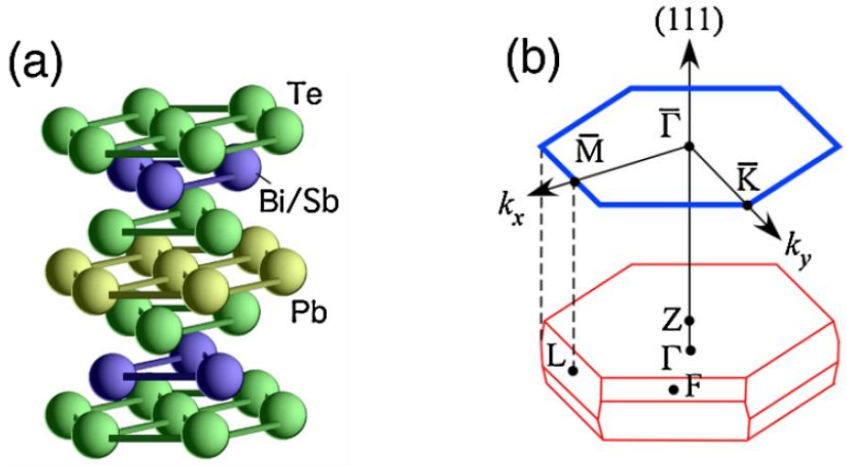

FIG. 4-1. (a) Crystal structure of $Pb(Bi_{1-x}Sb_x)_2Te_4$. (b) Bulk Brillouin zone (red thin lines) and corresponding (111) surface Brillouin zone (blue thick lines).

4.2 Experimental

Single crystals of $Pb(Bi_{1-x}Sb_x)_2Te_4$ except for x = 1.00 were grown by melting stoichiometric amounts of high purity elements (Pb 99.998%, Bi, Sb, and Te 99.9999%) in a sealed evacuated quartz tube at 900°C for 24 h, followed by cooling to 700°C in 5 h and subsequent slow cooling to 500°C in 100 h, and then switching off the furnace to cool it to room temperature. The resulting crystals are easily cleaved along the rhombohedral (111) plane to reveal a shiny surface. The grown crystals were characterized by x-ray diffraction (XRD) analysis on the cleaved surface and confirmed to be single phase. The x = 1 end member $PbSb_2Te_4$ is known to be difficult to synthesize from the stoichiometric composition [74,75]; therefore, $PbSb_2Te_4$ has been synthesized using Pb:Sb:Te molar ratio of 2:6:11. For this batch, the 900°C melt was cooled to room temperature at the rate of 48°C/h. The $PbSb_2Te_4$ phase was collected from the part of the boule which crystallized at the early stage of the growth, and its crystal structure has been confirmed by XRD.

Single crystals of $Pb(Bi_{1-x}Sb_x)_2Te_4$ with x =0.00, 0.40, and 1.00 have been measured by ARPES at the beam line BL28A at Photon Factory (KEK) using VGScienta SES2002 electron analyzer with a tunable synchrotron circularly polarized light in the energy range of 36–80 eV. The energy and angular resolutions have been set at 15–30 meV and 0.2°, respectively. A mirror-like (111) surface was obtained by *in situ* cleaving at T = 30 K just before the measurement in ultrahigh vacuum of 1×10^{-10} Torr, and kept at the same temperature during the measurement. ARPES data have been obtained by rotating the sample with respect to the electron analyzer using a high-precision five-axes manipulator equipped with a liquid helium cryostat. The Fermi level (E_F) of the samples was referenced to that of a gold film evaporated onto the sample holder. All the spectra were recorded within 12 h after cleaving, during which any sign of degradation or contamination of the sample surface was not observed. It was confirmed that the results are reproducible by measuring several samples.

For transport measurements, the grown crystals of $Pb(Bi_{1-x}Sb_x)_2Te_4$ with x = 0.00, 0.40, 0.55, 0.60, 0.80, and 1.00 have been cut and cleaved into a thin rectangular parallelepiped shape with a typical dimension of $2 \times 0.5 \times 0.2$ mm^3, and six gold wires were attached to each sample by a spot welding technique. The in-plane resistivity ρ_{xx} and the Hall resistivity ρ_{yx} were measured down to 1.9 K with the standard six-probe method using Quantum Design PPMS-9.

4.3 Results and Discussion

4.3.1 ARPES measurements on $PbBi_2Te_4$

Figures 4-2(a) and 4-2(b) show valence-band ARPES spectra of the end member $PbBi_2Te_4$ (x = 0.0) measured along high-symmetry lines $\bar{\Gamma}\bar{M}$ and $\bar{\Gamma}\bar{K}$ in the surface Brillouin zone, respectively. Corresponding energy distribution curves are also displayed in Figs. 4-2(c) and 4-2(d). In Figs. 4-2(a) and 4-2(b), several dispersive bands exist at the binding energy (E_B) of 0.5–4.5 eV. These bands are attributed to the hybridized states of Bi/Pb 6p and Te 5p orbitals [70–72]. As seen in the energy distribution curves along the $\bar{\Gamma}\bar{M}$ direction in Fig. 4-2(c), a hole-like band exists with the top of dispersion slightly away from the $\bar{\Gamma}$ point (see black arrow), which corresponds to the top of the valence band with the dominant Te 5p character, in agreement with the calculations which show a local maximum between Z and L points of the bulk Brillouin zone [71,72]. Such local maximum structure is not reproduced in the calculations without including spin-orbit coupling [71], suggesting that the observed valence-band feature is a fingerprint of the strong spin-orbit coupling. One can also see in Figs. 4-2(a) and 4-2(b) a weak intensity in the vicinity of E_F in the $\mathbf{k}$ region between the $\bar{\Gamma}$ and $\bar{M}$ points, which is assigned to the bulk conduction band of the strong Bi/Pb 6p character that lies above E_F in the calculations [70–72]. In the present ARPES experiment, this band is shifted downward to cross E_F, possibly owing to the electron-doped nature of as-grown crystals as in the case of other 3D topological insulators [20,21,34–36].

Figure 4-3(a) displays the ARPES intensity at E_F of $PbBi_2Te_4$ plotted as a function of 2D wave vector measured with $h\nu$ = 80 eV, which covers a wide $\mathbf{k}$ region in the surface Brillouin zone. In both the first and second Brillouin zones, one can see a circular-like Fermi surface centered at the $\bar{\Gamma}$ point together with elongated intensity patterns extending toward the $\bar{M}$ point. To elucidate the Fermi-surface topology and band dispersion around the $\bar{\Gamma}$ point in more detail, ARPES measurement was performed with higher energy resolution and finer $\mathbf{k}$ interval with $h\nu$=60 eV, and the result of the Fermi-surface mapping is shown in Fig. 4-3(b). Figs. 4-3(c) and 4-3(d) correspond to the band dispersions for the $\bar{\Gamma}\bar{K}$ and $\bar{\Gamma}\bar{M}$ directions in Figs. 4-3(c) and 4-3(d), respectively.

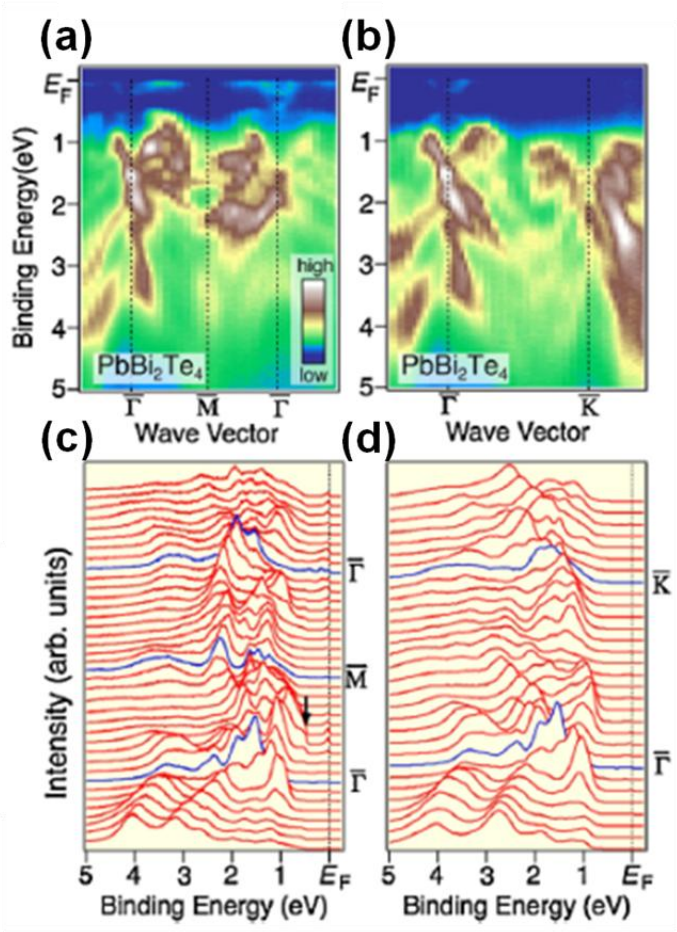

FIG. 4-2. (a),(b) ARPES intensity of $PbBi_2Te_4$ (x = 0.0) plotted as a function of E_B and wave vector along $\bar{\Gamma}\bar{M}$ and $\bar{\Gamma}\bar{K}$ high symmetry lines, respectively, measured with $h\nu$ = 80 eV. (c), (d) Corresponding energy distribution curves of (a) and (b), respectively.

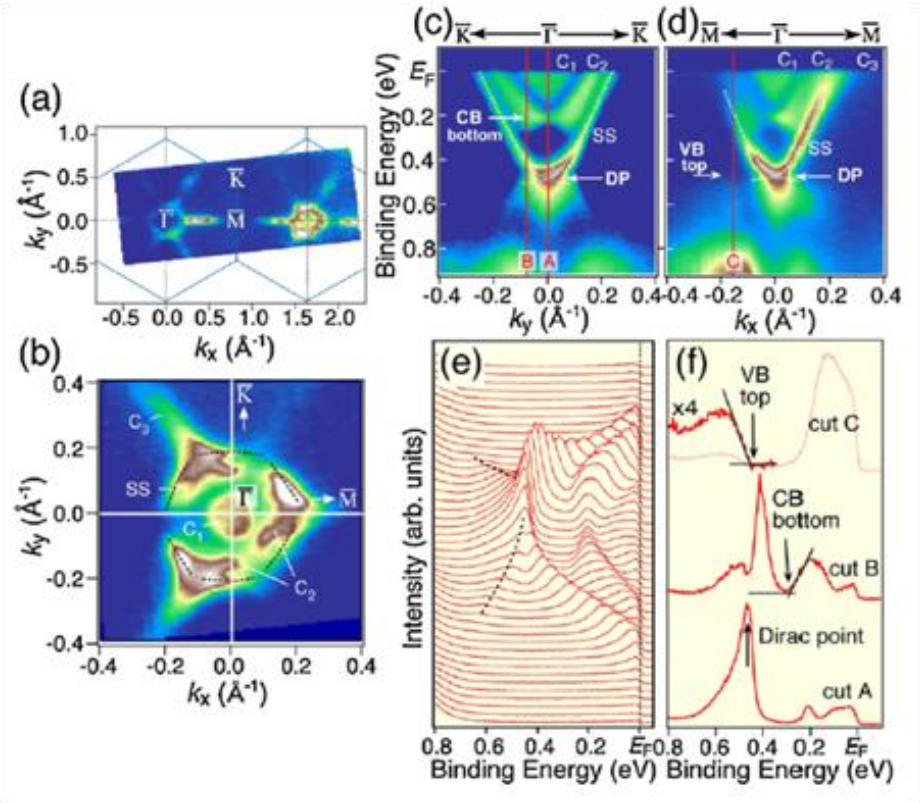

FIG. 4-3. (a) ARPES intensity plot at E_F of $PbBi_2Te_4$ (x = 0.0) as a function of 2D wave vector measured with $h\nu$ =80 eV. (b) 2D intensity plot at E_F around the $\bar{\Gamma}$ point measured with $h\nu$ = 60 eV. (c),(d) Near-E_F ARPES intensity as a function of E_B and wave vector along $\bar{\Gamma}\bar{M}$ and $\bar{\Gamma}\bar{K}$ cuts, respectively [white lines in (b)]. Dashed lines are a guide to the eyes to trace the surface states (SS); CB, VB, and DP stand for conduction band, valence band, and Dirac point, respectively. (e) Corresponding energy distribution curves along the $\bar{\Gamma}\bar{K}$ direction. (f) Plot of energy distribution curves at **k** points A–C as indicated by red lines in (c) and (d).

As clearly seen in the ARPES intensity of Fig. 4-3(c), the sharply dispersive "*V*"-shaped electron-like surface state (denoted SS) was observed, whose bottom is located at E_B~0.5 eV. A careful look at energy distribution curves in Fig. 4-3(e) further reveals the presence of an additional branch of band showing hole-like dispersion centered at the $\bar{\Gamma}$ point (traced by dashed lines). This branch merges into the *V*-shaped band exactly at the $\bar{\Gamma}$ point, satisfying the Kramers degeneracy and forming a deformed Dirac-cone dispersion as in Bi_2Te_3 [21]. The surface origin of these branches was confirmed by the fact that the energy position is stationary with the variation of $h\nu$. Note that the energy position of other bands was also found to be insensitive to the $h\nu$ variation in the present range of $h\nu$, presumably because of the quasi-two-dimensional character of electronic states due to the long *c* axis. Nevertheless, the observed gapless dispersion should belong to the surface states, since it does not show up in the bulk band calculations of $PbBi_2Te_4$ [70,72].

One can also see in Figs. 4-3(c) and 4-3(d) two electron-like bands within the surface states near E_F which exhibit a parabola-like (C_1) and "*w*"-shaped (C_2) dispersions, corresponding to a small circular pocket and a larger pocket with triangular-like intensity distribution, respectively, in Fig. 4-3(b). Furthermore, in Figs. 4-3(b) and 4-3(d) another weak intensity (C_3) is seen outside of the surface states which either form an elongated pocket or are connected to the C_2 band along the $\bar{\Gamma}\bar{M}$ direction, although it is hard to experimentally conclude which is the case because of the presence of multiple bands in the close vicinity of E_F as well as the possible surface resonance which smears the overall intensity distribution in this **k** region. The C_1-C_3 bands are attributed to the bulk conduction band, and the bottom of the lowest-lying conduction band is located at the **k** region where the C_2 band exhibits a local minimum structure, as indicated by a red line for cut B in Fig. 4-3(c). Finally, in Fig. 4-3(d) the highest-lying bulk valence band has its local maximum slightly away from the $\bar{\Gamma}$ point (at cut C), suggesting an indirect nature of the bulk band gap.

The bulk band gap was quantitatively estimated by determining the leading (trailing) edge of the valence (conduction) band, as shown by an arrow in Fig. 4-3(f). The energy location of the conduction-band bottom and the valence-band top are ~0.25 and ~0.45 eV, respectively, corresponding to the band-gap size of ~0.2 eV, slightly larger than that of the band calculations (0.1–0.15 eV) [70-72]. Moreover, as seen in the energy distribution curve for cut A, the Dirac point (at E_B = 0.46 eV) is situated at almost the same energy as the valence-band top. The band velocity at the

Dirac point, v_{Dirac}, was estimated to be 1.0 eV Å along the $\bar{\Gamma}\bar{M}$ direction, which is only about 35–50% of the value obtained for Bi_2Te_3 and $TlBiSe_2$ (2.7 eV Å [21] and 2.0 eV Å [34], respectively).

The Fermi surface and band diagrams for the bulk and surface bands are shown in Fig. 4-4(a), obtained from the present ARPES experiment. One can see the complex and anisotropic nature of the conduction band, which is distinctly different from prototypical topological insulators [20,21] showing a weaker anisotropy in the conduction band, likely because of the heavily electron-doped nature of $PbBi_2Te_4$ as apparent from the deeper energy position of the Dirac point as compared to other topological insulators [20,21,34,35]. One can have a clear view of the 2D band dispersion in Fig. 4-4(b) where the ARPES intensity for x = 0.0 is plotted as a function of k_x and k_y for several E_B's. The triangular-shaped intensity pattern at E_F, which is dominated by the contribution from the C_2 band, gradually diminishes upon approaching the Dirac point. At E_B = 0.3 eV, one can recognize a strongly deformed ring-like intensity pattern which originates from the surface states. This ring-like image shrinks and converges into a single bright spot at the Dirac point (E_B = 0.46 eV), and then expands again below the Dirac point (E_B = 0.5 eV), as expected from the Dirac-cone energy dispersion. At E_B = 0.5 eV, one can notice an additional weak intensity extending toward the $\bar{M}$ point, which originates from the top of the valance band as also seen in Fig. 4-3(d). To discuss the shape of the Dirac band in more detail, the **k** location of the band crossing point is quantitatively estimated in various E_B slices above the Dirac point, and a representative result is displayed in Fig. 4-4(c). Obviously, the contour map of the band dispersion signifies the hexagonal warping which appears to become more prominent as one moves away from the Dirac point, similarly to the case of other topological insulators [24,34,35,76].

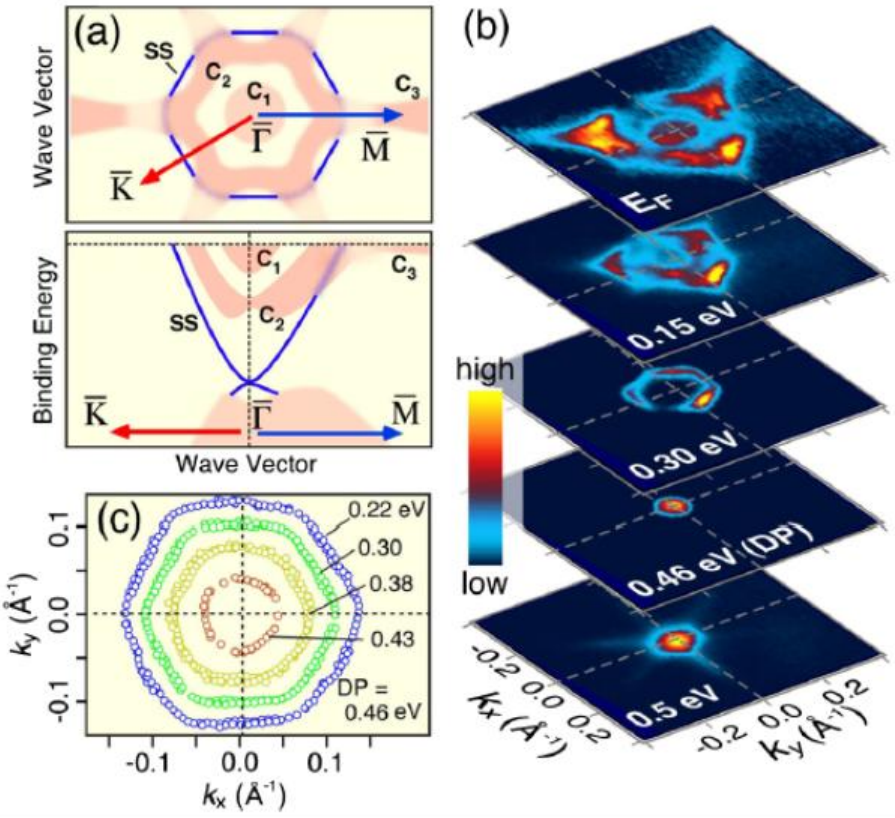

FIG. 4-4. (a) Schematic diagrams for (top) the Fermi surface and (bottom) the band dispersion of $PbBi_2Te_4$ obtained from the present ARPES experiment. For the bulk conduction and valance bands, a finite k_z dispersion and momentum broadening have been taken into account. (b) ARPES intensity plots for various E_B's between E_F and 0.5 eV. (c) Energy contour plots of the surface states for various E_B's estimated by tracing the peak position of momentum-distribution curves.

4.3.2 ARPES measurements on $Pb(Bi_{1-x}Sb_x)_2Te_4$, (x = 0.0, 0.4, and 1.0)

In this section, the evolution of the electronic states upon Sb substitution for Bi in $Pb(Bi_{1-x}Sb_x)_2Te_4$ is described. Figures 4-5(a) to 4-5(c) display plots of near-E_F ARPES intensity around the $\bar{\Gamma}$ point as a function of E_B and $\mathbf{k}$, corresponding energy distribution curves, and the Fermi-surface mapping, for x = 0.0, 0.4, and 1.0, respectively. The band dispersions for x = 0.4 appear to be quite similar to that for x = 0.0, although the overall dispersive features are shifted upward by ~0.15 eV. The C_1 band has completely disappeared in the ARPES intensity, as one can also confirm in the absence of the C_1 pocket in Fig. 4-5(c). The C_3 Fermi surface also vanishes at x = 0.4. At x = 1.0 ($PbSb_2Te_4$), on the other hand, the overall spectral feature appears to be quite different from those at x = 0.0 and 0.4. In Fig. 4-5(a), one can see a hole-like band with a weak intensity at E_B= 0–0.3 eV, together with a less dispersive bright intensity pattern at ~0.6 eV. The former band is assigned to the bulk valance band which is seen at E_B= 0.4–0.6 eV at x = 0.4, whereas the latter band is one of the valance bands which corresponds to the feature at ~1.0 eV for x = 0.0 [see Figs. 4-2(a)–4-2(c)], suggesting that the Dirac point for x = 1.0 is located in the unoccupied region.

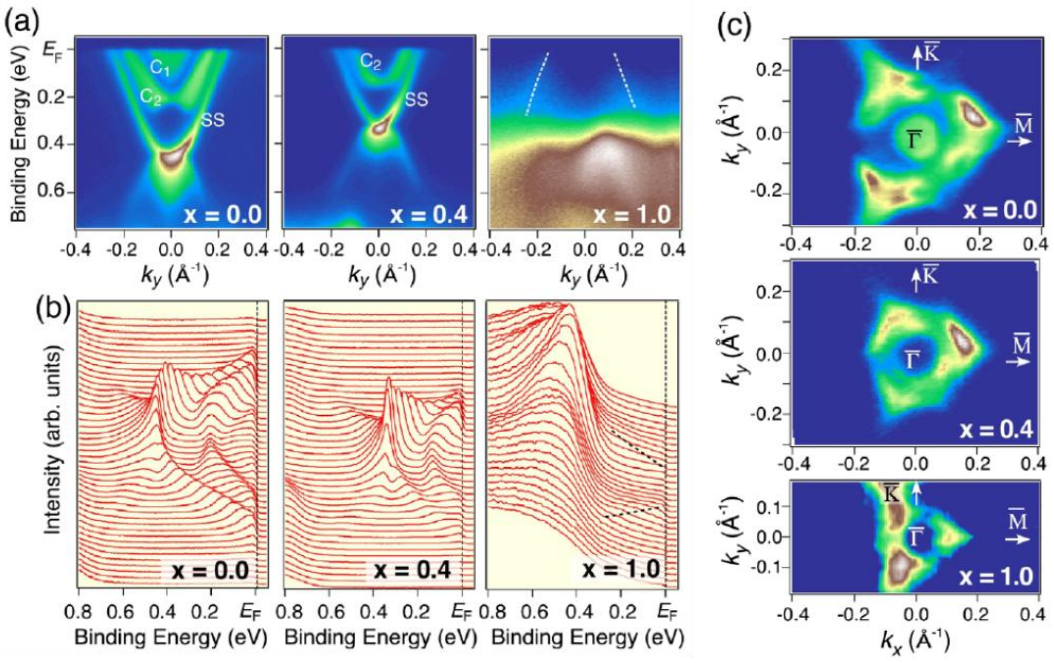

FIG. 4-5. (a)–(c) Comparison of (a) the near-EF band dispersions, (b) the energy distribution curves, and (c) the Fermi surface in $Pb(Bi_{1-x}Sb_x)_2Te_4$ for three x values (x=0.0, 0.4, and 1.0).

To quantitatively evaluate the evolution of the electronic states upon Sb substitution, the band dispersions are shown in Fig. 4-6(a) which were determined from the peak positions in the energy- or momentum-distribution curves. One can recognize that the energy shift of the surface states and bulk bands proceeds roughly in a rigid-band manner since the bands for different x values nearly overlap with each other when their energy positions are plotted with respect to the Dirac-point energy, despite the total μ shift of as large as 0.6 eV. Indeed, the band dispersion below E_F for x = 1.0 suggests that the Dirac point is located above E_F by ~50 meV, pointing to the sign change of Dirac carriers from *n* type to *p* type at some x between 0.4 and 1.0, in agreement with the Hall coefficient which exhibits a negative value at x = 0.0–0.4 and a positive value at x = 1.0. The present result thus demonstrates that the substitution of Bi with Sb results in the μ shift without significantly altering the shape of the Dirac surface state, as highlighted in the schematic band picture in Fig. 4-6(b).

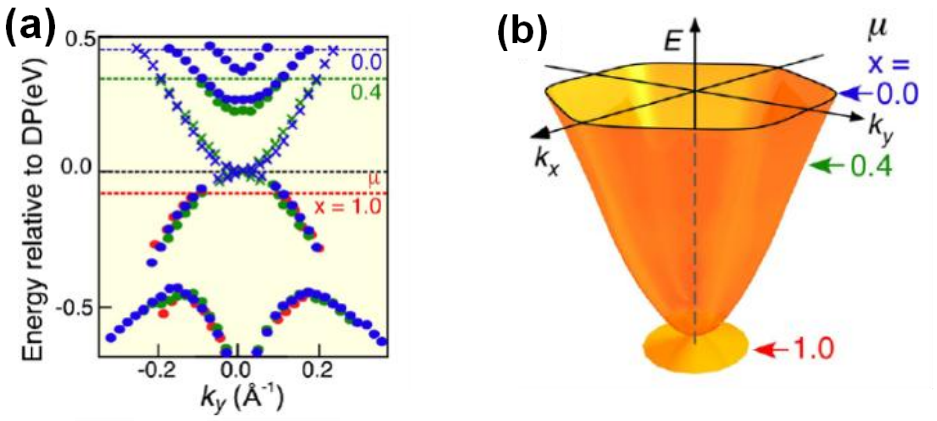

FIG. 4-6. (a) The bulk (circles) and surface (crosses) band dispersions relative to the Dirac point in the $Pb(Bi_{1-x}Sb_x)_2Te_4$ system for three x values (x = 0.0, 0.4, and 1.0), estimated by tracing the peak positions of energy- and momentum-distribution curves. The locations of the chemical potential for the three compositions with respect to the Dirac point are shown by horizontal dashed lines. (b) Schematic 3D picture of the Dirac-band surface state and the position of μ for each x.

The experimental realization of the sign change of Dirac carriers points to the high potential of Pb-based ternary chalcogenides for investigations of various novel topological phenomena which require the control of Dirac carrier conduction. This system would also provide an excellent platform for the development of novel topological devices with *p*-*n* junction configurations that are essential for various applications as in semiconductor technology as well as with dual-gate configuration for the electric control of spins [77]. Moreover, the observed variation in the chemical-potential value of ~0.6 eV as achieved by the Bi/Sb replacement, which is the largest among known topological insulators, is useful for varying the Dirac carrier concentrations in a wide range, though bulk carriers coexist in most of the ranges. A next important step would be to synthesize a truly bulk insulating sample, which could be accessible by a fine control of the Bi/Sb ratio in the crystal. In the following sections, the effects of the Bi/Sb replacement on various materials properties are carefully examined.

4.3.3 XRD measurements on the cleaved surfaces of $Pb(Bi_{1-x}Sb_x)_2Te_4$

Figure 4-7(a) shows the XRD patterns measured on the cleaved surfaces of $Pb(Bi_{1-x}Sb_x)_2Te_4$ single crystal samples. One can index the observed peaks of all the samples based on the rhombohedral structure with $R\bar{3}m$ space group [74], which confirms that this solid-solution system keeps the same crystal structure from x = 0 to 1. From these XRD data, the lattice constant *c* is estimated to be 4.149(3) nm for x = 0.00 and 4.169(3) nm for x = 1.00, both of which are consistent with the literature [73,74]. One can see that the *c* parameters of the crystals in the intermediate compositions lie in between these two values, but they do not change linearly; in particular, the *c* parameters for x = 0.40 – 0.60 are nearly independent of x, as shown in Fig. 4-7(b). This apparent violation of the Vegard's law is probably related to the fact that the defect chemistry in this compound is complicated [75] and a large numbers of defects (both substitutional and antisite) are present; if the nature of defects and/or their density changes with x, the Vegard's law can be violated. Nevertheless, as shown in Fig. 4-7(c), the width of the prominent (009) peak remains essentially unchanged with x, indicating that the crystalline quality is kept reasonably high even in the mixed compositions.

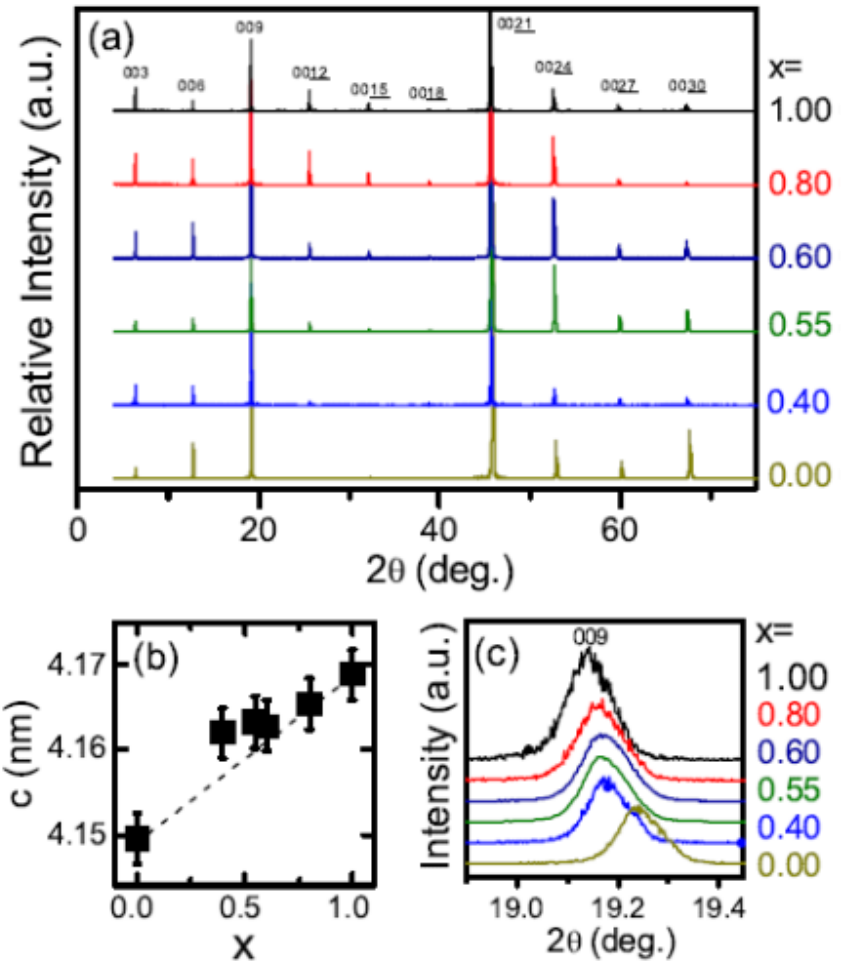

FIG. 4-7. (a) XRD patterns measured on (111) cleaved surfaces of $Pb(Bi_{1-x}Sb_x)_2Te_4$ single crystals. The indices are assigned based on the $R\bar{3}m$ space group. (b) x dependence of the *c* lattice parameter, showing apparent violation of the Vegard's law; the dashed line shows the putative Vegard's law line. (c) Magnifications of the XRD data near the (009) peak for all the x values.

The actual compositions of the crystals for each batch have been measured using inductively-coupled plasma atomic-emission spectroscopy (ICP-AES). The measured ratio between Sb and Bi turned out to be close to the nominal value x within $\Delta x \simeq 0.015$; therefore, each sample was labeled with the nominal x value. The result of the ICP-AES analyses is summarized in Table 4-I, which also shows the detailed composition of each batch in terms of $Pb_a(Bi_{1-x}Sb_x)_yTe_z$. One can see significant deviations from the stoichiometric composition, which is consistent with the previous finding [78] that there are large numbers of substitutional and antisite defects in this material.

TABLE 4-I: Actual compositions of the grown crystals measured by ICP-AES analyses and expressed in terms of $Pb_a(Bi_{1-x}Sb_x)_yTe_z$. If there were no substitutional defects, one would have $a = 1$, $y = 2$, and $z = 4$.

x (nominal)	x (actual)	a (Pb)	y (Bi+Sb)	z (Te)
0.00	0.000	0.799	1.940	4.261
0.40	0.415	0.787	1.972	4.241
0.55	0.554	0.744	1.957	4.299
0.60	0.610	0.912	2.132	3.957
0.80	0.797	0.749	2.249	4.002
1.00	1.000	0.665	2.061	4.274

4.3.4 Transport measurements of $Pb(Bi_{1-x}Sb_x)_2Te_4$

Figure 4-8(a) shows temperature dependences of ρ_{xx} for all the compositions studied. The x dependence of the carrier concentration n_{3D}, estimated from the Hall coefficient at 1.9 K, is shown in Fig. 4-8(b); here, n_{3D} is negative when the carriers are *n*-type. One can immediately see in Fig. 4-8(b) that a sign change in the bulk carriers occurs between x = 0.55 and 0.60. However, the absolute value of n_{3D} remains high ($>10^{20}$ cm^{-3}) across the transition, which explains the metallic $\rho_{xx}(T)$ behavior observed in all the samples. The observed x dependencies of n_{3D} and the Hall mobility μ_H are summarized in Table 4-II.

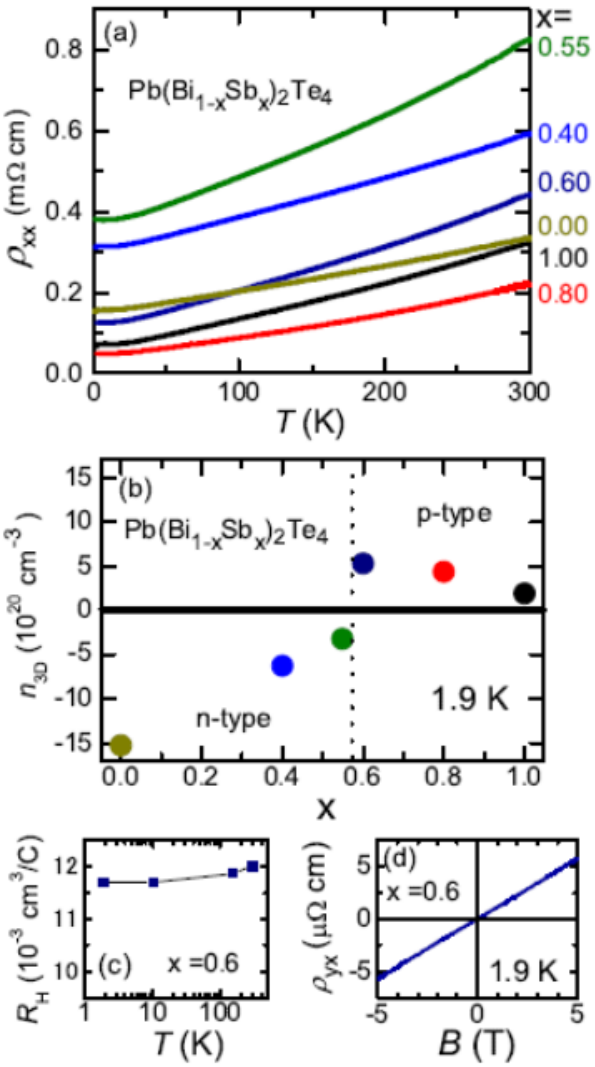

FIG. 4-8. (a) Temperature dependences of ρ_{xx} measured in a series of $Pb(Bi_{1-x}Sb_x)_2Te_4$ single crystals. (b) x-dependence of the carrier concentration n_{3D}, which is estimated from the Hall coefficient R_H at 1.9 K. (c) Temperature dependence of R_H for x = 0.60. (d) Magnetic-field dependence of ρ_{yx} at 1.9 K for x = 0.60.

TABLE 4-II: Type of carriers, carrier density n_{3D}, and the Hall mobility μ_H, measured in $Pb(Bi_{1-x}Sb_x)_2Te_4$ single crystals with various x values. For *n*-type carriers, n_{3D} is shown in negative values.

x (nominal)	x (actual)	type	n_{3D} (cm^{-3})	μ_H (cm^2/Vs)
0.00	0.000	n	-16×10^{20}	59
0.40	0.415	n	-6.3×10^{20}	31
0.55	0.554	n	-3.2×10^{20}	50
0.60	0.610	p	5.3×10^{20}	93
0.80	0.797	p	4.3×10^{20}	233
1.00	1.000	p	1.9×10^{20}	472

The Hall coefficient R_H shows only a weak temperature dependence, and in Fig. 4-8(c) typical temperature dependence data are shown for x = 0.60. The magnetic field dependence of ρ_{yx} was always found to be essentially linear, as shown in Fig. 4-8(d) as an example. This suggests the dominance of only one band at each composition.

The large swing in n_{3D} from -3.2×10^{20} cm^{-3} to $+5.3\times10^{20}$ cm^{-3} upon changing x from 0.55 to 0.60 indicates that the chemical potential in $Pb(Bi_{1-x}Sb_x)_2Te_4$ is always pinned to bulk bands, and tuning it into the band gap is a difficult task. This difficulty is probably related to the nature of the defects in $Pb(Bi_{1-x}Sb_x)_2Te_4$, that is, the major ones are substitutional and antisite defects, not vacancies [78]. From the crystal growth point of view, suppressing substitutional or antisite defects are much more difficult than suppressing vacancies. It is useful to note that the defect chemistry in $Pb(Bi_{1-x}Sb_x)_2Te_4$ is similar to that in Bi_2Te_3 [79], where it is impossible to make it insulating simply by tuning the composition or the growth condition even though one can change the carrier types [21,80]. Therefore, to achieve the intrinsic topological insulator regime in the $Pb(Bi_{1-x}Sb_x)_2Te_4$ system, one would need to find a suitable dopant that would compensate for the naturally-doped bulk carriers and create an appropriate impurity state within the bulk band gap to pin the chemical potential.

4.4 Conclusions

In this chapter, I described the ARPES and transport experiments of single crystalline $Pb(Bi_{1-x}Sb_x)_2Te_4$ samples. Direct evidence for the existence of the Dirac-cone topological surface state within the indirect bulk band gap is found. Moreover, a sign change of charge carriers from *n*-type to *p*-type upon variation of the Sb concentration is observed. It is also found that this transition in the carrier type occurs between x = 0.55 and 0.60, while the bulk carrier density remains always high and the system remains metallic even near the *n*- to *p*-type transition. This behavior is most likely related to the fact that major defects are substitutional and antisites, both of which are difficult to suppress for thermodynamic reasons. Therefore, it is necessary to find a suitable dopant to achieve the intrinsic topological insulator regime in this system.

Chapter 5 Natural Heterostructures of Topological Insulators in $(PbSe)_5(Bi_2Se_3)_{3m}$

5.1 Introduction

The topological surface state is characterized by a Dirac-like linear energy dispersion with a helical spin texture. Owing to the peculiar spin texture, the Dirac fermions on the surface of topological insulators (TIs) are immune to backward scattering by nonmagnetic impurities or disorder and carry dissipationless spin current, holding promise for exploring fundamental physics, spintronics, and quantum computing. However, there are a number of challenges that need to be overcome before TIs meet those promises, as mentioned in Chapter 1. Furthermore, it turned out to be difficult to maintain stable surface properties under ambient atmosphere [81,82]. Also, potential applications of TIs for a wide range of devices working at room temperature require a large bulk band gap, but the gap value reported to date is ~0.35 eV at most [34]. Such situation has been a hindrance for realizing novel topological phenomena and device applications of TIs, calling for a conceptually new approach to the manipulation of material properties of TIs.

A commonly used strategy for such a manipulation is the chemical substitution of constituent elements, as has been widely tried in systems based on Bi_2Se_3 and Bi_2Te_3 [30,81]. Another, potentially more effective approach is the heterostructure engineering where one can alter the stacking sequence of layers or insert different building blocks into the crystal, which may trigger gigantic quantum effects and/or new physical phenomena. However, this route has not been seriously explored in 3D TIs owing to a limited number of TI materials discovered to date.

In tetradymite Bi_2Se_3, the ordered Se-Bi-Se-Bi-Se quintuple layer (QL) forms the basic unit, which is stacked along the (111) direction. In the case of the Pb-based homologous-series compounds whose chemical compositions can be expressed as $[(PbSe)_5]_n[(Bi_2Se_3)_3]_m$, the monoclinic crystalline structure consists of m QLs of Bi_2Se_3 sandwiched by adjacent n bilayers of PbSe [83-85] as shown in Fig. 5-1, which offers an excellent example to systematically alter the building blocks of the crystal. Therefore, this system is suitable for investigating new functional properties of TIs.

In this chapter, it will be shown that utilization of naturally occurring heterostructures in bulk crystals containing TI units might be a promising pathway to overcome the aforementioned problems of currently available TI materials. ARPES measurements were performed for a fixed n value (n = 1) with m = 1 ($Pb_5Bi_6Se_{14}$) and m = 2 ($Pb_5Bi_{12}Se_{23}$). The data are compared with those for Bi_2Se_3, which can be viewed as a member of this homologous series with (n,m) = (1, ∞). It was demonstrated that this lead (Pb)-based homologous series, $(PbSe)_5(Bi_2Se_3)_{3m}$, indeed forms a natural multilayer heterostructure consisting of a TI and an ordinary insulator. Furthermore, ARPES data suggest that quantum confinement effects due to the characteristic layer stacking of this homologous series result in the "capping" of the topological states, giving the largest bulk band gap among known TIs. In addition, the states near the Fermi energy were found to present a drastic change between m = 1 and m = 2, probably reflecting a band inversion in the Bi_2Se_3 unit.

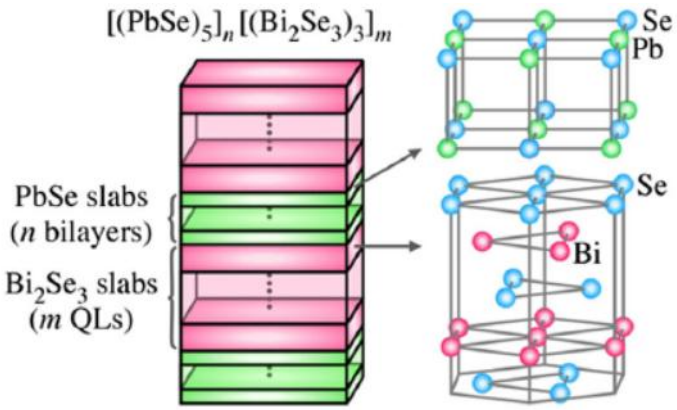

FIG. 5-1. Schematic illustration of the building blocks of $[(PbSe)_5]_n[(Bi_2Se_3)_3]_m$ homologous series.

5.2 Experimental

Single crystals of $(PbSe)_5(Bi_2Se_3)_{3m}$ were grown by a modified Bridgman method using highly pure elements (Pb 99.998%, Bi and Se 99.9999%) in a sealed evacuated quartz tube. The phase diagram of the Pb-Bi-Se ternary system is very complicated [85], which causes various crystal phases to compete during the crystal growth and one typically finds multiple phases in a boule grown by the Bridgman method. For this experiment, the starting composition was chosen to be Pb:Bi:Se = 2:2:5, and after the growth, the dominant phase in the boule was found to be different for the top and bottom parts of the boule. Crystal consisting of the targeted phase (i.e., m = 1 or 2) were chosen based on the x-ray diffraction analysis of the pieces cut out from the boule [85]. Nevertheless, it turned out that a finite admixture of different phases in the bulk crystal is unavoidable (e.g., a few percent of m = 2 domains are mixed in the m = 1 sample as confirmed by the x-ray diffraction measurement) [86]. Hence, a light beam in ARPES measurements was focused on a small spot (~ 0.1 mm) and scanned the beam-spot position on the cleaved surface to make sure that the ARPES data are taken on a single domain of the desired phase. It was confirmed that the ARPES data from the same domain give essentially the same result even when the nominal composition of the bulk crystal is different. ARPES measurements have been performed using a VG-Scienta SES2002 electron analyzer with a tunable synchrotron light at the beam line BL28A at Photon Factory (KEK). Circularly polarized light with energies in the range of 36–60 eV has been used for the measurements. The energy and angular resolutions have been set at 15–30 meV and 0.2°, respectively. Samples were cleaved in situ along the (111) crystal plane in an ultrahigh vacuum of 1×10^{-10} Torr. A shiny mirror-like surface was obtained after cleaving the samples, confirming their high quality. The Fermi level (E_F) of the samples was referenced to that of a gold film evaporated onto the sample holder.

5.3 Results and Discussion

Figure 5-2 shows the valence-band ARPES intensity maps for m = 1, 2 and ∞ as a function of the binding energy (E_B) versus momentum ($\mathbf{k}$) measured along the $\bar{\Gamma}\bar{K}$ cut of the Brillouin zone. They exhibit common characteristics below E_B of ~1 eV, suggesting that the spectral features for m = 1 and 2 are essentially dominated by the contribution from the Bi_2Se_3 layer. A closer look reveals that the overall band dispersions for m = 1 and 2 are shifted downward with respect to that for m = ∞, likely due to an increase in Se vacancies caused by Pb substitution as also reported for other Pb-based TIs [87,88]. The dominant contribution from the Bi_2Se_3 layer is also confirmed by the measurements of core levels. As shown in Fig. 5-3, the intensity of Pb-5d core levels is much weaker than that of Bi 5d in both m = 1 and 2, while their photo-ionization cross sections are similar [89]. This is likely to indicate that the topmost layer of the cleaved surface is the Bi_2Se_3 QL in the present experimental condition. Moreover, the Pb-5d intensity observed for m = 2 is much weaker than that for m = 1 (right inset), and this can be naturally understood if the top PbSe layer is located deeper beneath the surface in the m = 2 case (see left inset). In fact, a rough estimate that takes into account the finite photoelectron escape length (0.5 nm) and the depth of the topmost PbSe layer (1 and 2 nm for m = 1 and 2, respectively) suggests an order of magnitude weaker Pb-5d intensity for m = 2, which is in line with the present experimental result. The downside of this situation is that one cannot measure the confinement effect in the PbSe unit and its resultant band gap, which is 0.27 eV in bulk PbSe.

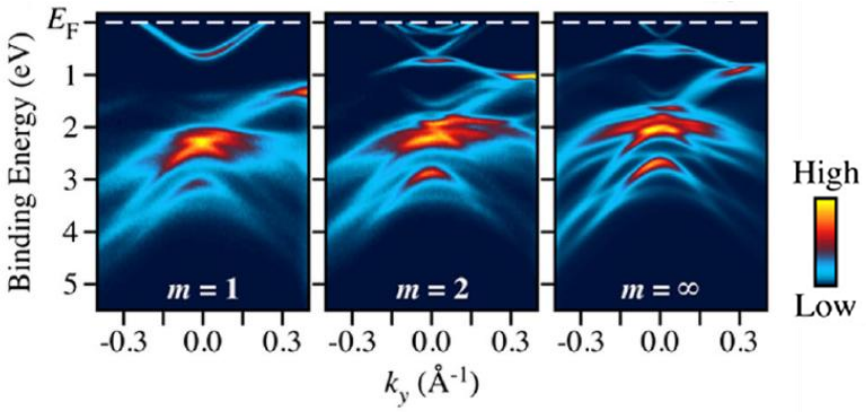

FIG. 5-2. Comparison of the valence-band ARPES intensities of $(PbSe)_5(Bi_2Se_3)_{3m}$ for $m = 1$, 2 and ∞, plotted as a function of E_B and wave vector measured along the k_y axis (the $\bar{\Gamma}\bar{K}$ cut) at $T = 30$ K with $h\nu = 60$ eV.

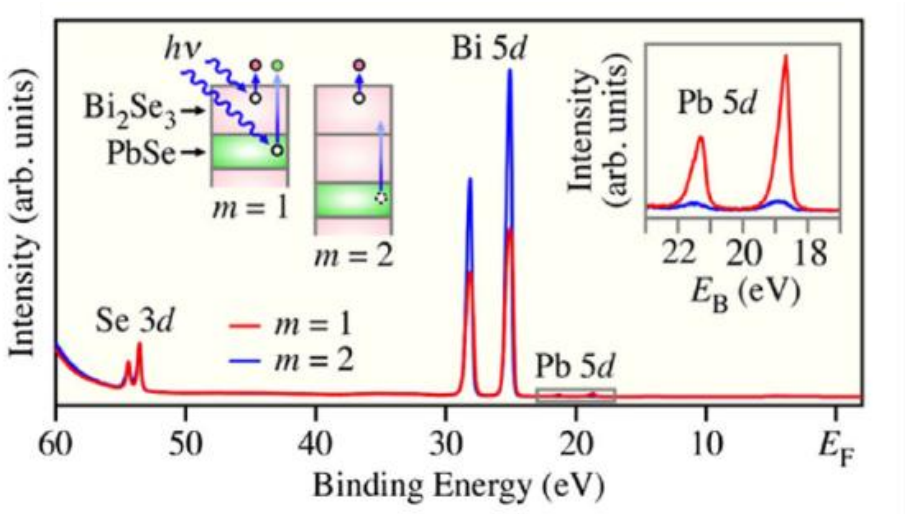

FIG. 5-3. Normal-emission photoemission spectra in a wide energy region for $m = 1$ and 2 measured with $h\nu = 60$ eV at $T = 30$ K. The right-hand-side inset shows a magnified view around the Pb-5d core levels. Schematic illustration of the cleaved surface and the photoemission process for $m = 1$ and 2 is also displayed in the left-hand-side inset.

A side-by-side comparison of the band dispersions near E_F in Figs. 5-4(a) and 5-4(b) clearly shows a marked difference in m = 1, 2 and ∞. Specifically, the band structure for m = 1 contains a single, parabolic electron-like band, while that for m = 2 is composed of multiple bands. The band structure at m = 2 is also distinct from that at m = ∞, where a simple X-shaped Dirac-cone surface state shows up. It is most likely that such a striking difference in the near-E_F electronic states originates from the difference in the number of Bi_2Se_3 QLs in a unit cell, which is inferred from the fact that the ARPES data for m = 1 and 2 bear spectral signatures resembling those of Bi_2Se_3 ultrathin films [90]; namely, the m = 1 data show only the upper parabola, as was the case for 1-QL film, and the m = 2 data present a gap with the lower band having a shallow dip at the top, similarly to the case for 2-QL film. This strongly suggests that the electronic states for m = 1 and 2 are quantized due to electron confinement within the Bi_2Se_3 layer, which would be expected in view of the insulating nature of the PbSe block layer indicated by the absence of any additional E_F crossing bands.

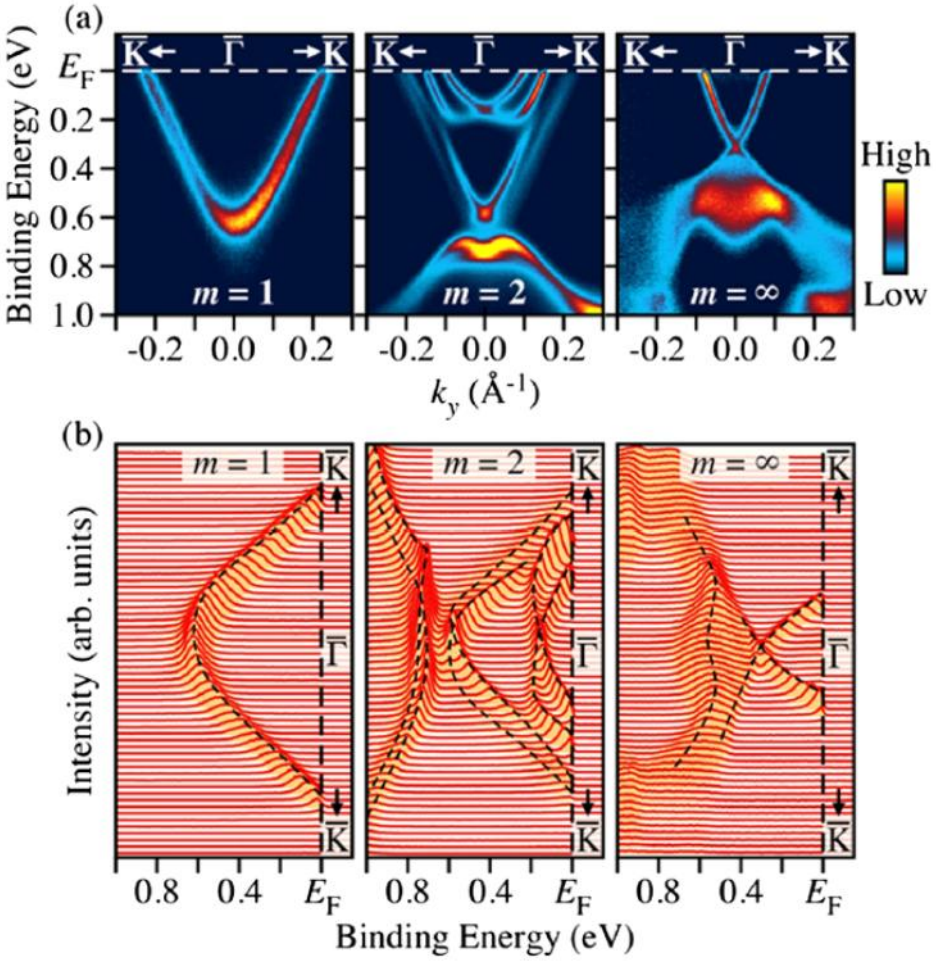

FIG. 5-4. (a),(b) Comparison of near-E_F ARPES intensities (a) and corresponding energy dispersion curves (b). Dashed curves in (b) are a guide to the eyes.

To gain further insights into the origin of the difference between m = 1 and 2, it is useful to examine the m = 2 data in detail. As shown in Figs. 5-5(a) and 5-5(b), the near-E_F dispersions for m = 2 are composed of six dispersive features labeled A–F, all of which show no photon-energy dependence, signifying negligible dispersion along the momentum perpendicular to the surface (k_z) and hence their 2D nature. The electron-like bands A and B cross at the $\bar{\Gamma}$ point at E_B = 0.16 eV and form two concentric Fermi surfaces [A and B in Fig. 5-5(c)], which indicates that their origin is the quantized bulk conduction bands with Rashba splitting [91,92]. The bands C and D in Fig. 5-5(a) are more dispersive than the bands A and B and cross E_F outside the bands A and B. They should essentially originate from the topological Dirac-cone states because (i) their overall dispersions overlap with the Dirac-cone surface states for m = ∞ [see Fig. 5-5(b)] and (ii) the corresponding Fermi surfaces [C and D in Fig. 5-5(c)] exhibit a hexagonal deformation similar to the case of m = ∞ [21,76]. It is therefore most natural to interpret that the bands C, D, E, and F originally arise as two topological interface states of the 2-QL Bi_2Se_3 unit at its top and bottom, but the proximity of the top and bottom interfaces causes the two topological states to hybridize and open a gap [90,93,94]; furthermore, those hybridized states are Rashba split due to the inversion-symmetry breaking at the surface. In fact, the bands C and D seem to smoothly connect to bands E and F, respectively, at the higher E_B side (see the schematic in Fig. 5-7). Note that the Rashba splitting in the upper branch of the hybridized topological states has already been reported in ultrathin films [90]. The present result is probably the first observation of the existence of topological states at the heterostructure interface of a bulk crystal. It should be noted that while bands C–F for m = 2 essentially originate from the topological states, the m = 2 system is not strictly topological because of the presence of a gap in the topological states and the even number of E_F crossings of the bands between two time-reversal-invariant momenta (i.e., the $\bar{\Gamma}$ and $\bar{M}$ points). In this context, the m = 2 phase is similar to a typical Rashba system.

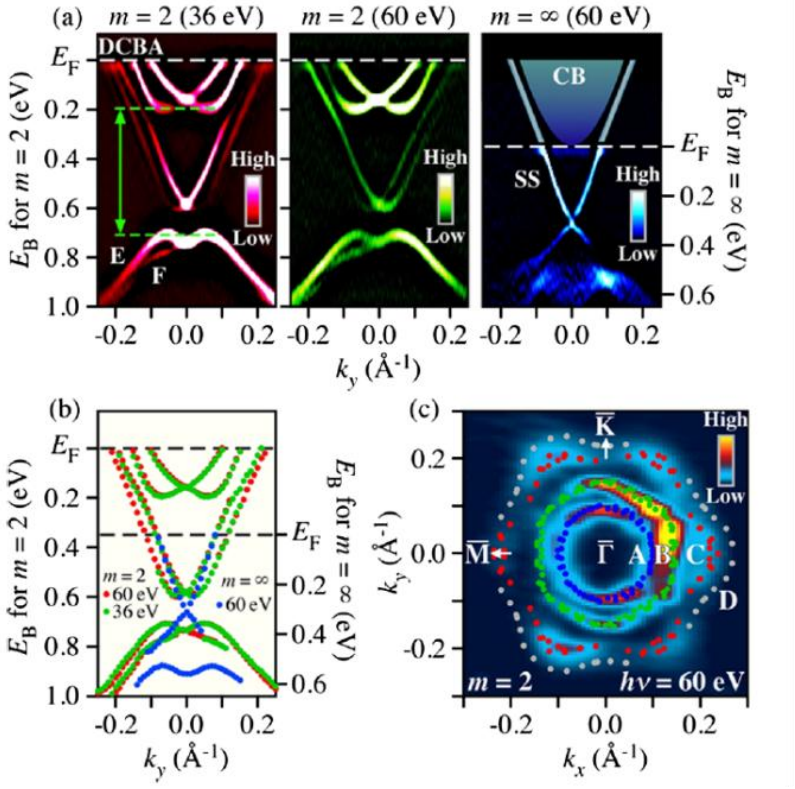

FIG. 5-5. (a) Second-derivative ARPES intensities near the $\bar{\Gamma}$ point for $m = 2$ plotted as a function of k_y and E_B measured at $h\nu =$ 36 (left) and 60 eV (center), compared to that for $m = \infty$ (right, measured with $h\nu = 60$ eV) which is shifted downward by 0.35 eV to take into account the doping difference. Gray (green) arrows and dashed lines depict a conservative estimate of the bulk band gap of 0.5 eV, judged from the energy difference between the edges of the bands B and E. Notice that band E is likely of the surface origin and, hence, the true bulk band gap may well be larger than 0.5 eV. The band dispersions expected for $m = \infty$ above E_F are also illustrated. (b) Direct comparison of the band dispersions obtained from the peak positions in the energy distribution curves for $m = 2$ and ∞; the dispersions for $m = \infty$ are shifted downward to account for the doping difference. (c) ARPES intensity mapping at E_F for $m = 2$ plotted as a function of 2D wave vector. The intensity is obtained by integrating the spectral intensity within ±10 meV of E_F. The Fermi vector of each pocket is plotted by dots.

The next important issue is the origin of the marked difference between m = 1 and 2. As discussed above, the 2D states C, D, E, and F observed for m = 2 are most likely of topological origin. In contrast, the parabola observed near E_F for m = 1 does not have a corresponding lower branch, which can also be seen in the isoenergy cuts of the spectra shown in Fig. 5-6, suggesting that its origin is distinct from a gapped Dirac cone. In Ref. 90, the absence of the lower branch in the 1-QL film was proposed to be due to bonding with the substrate; similarly, it is reasonable to speculate that the standard model Hamiltonian [19] is no longer applicable to 1 QL of Bi_2Se_3 sandwiched by PbSe layers and the band inversion is not taking place at the $\bar{\Gamma}$ point (a similar conclusion was also proposed in Ref. 95). In this case, the observed parabola for m = 1 is simply the degenerate lowest subband of the quantum confined conduction band.

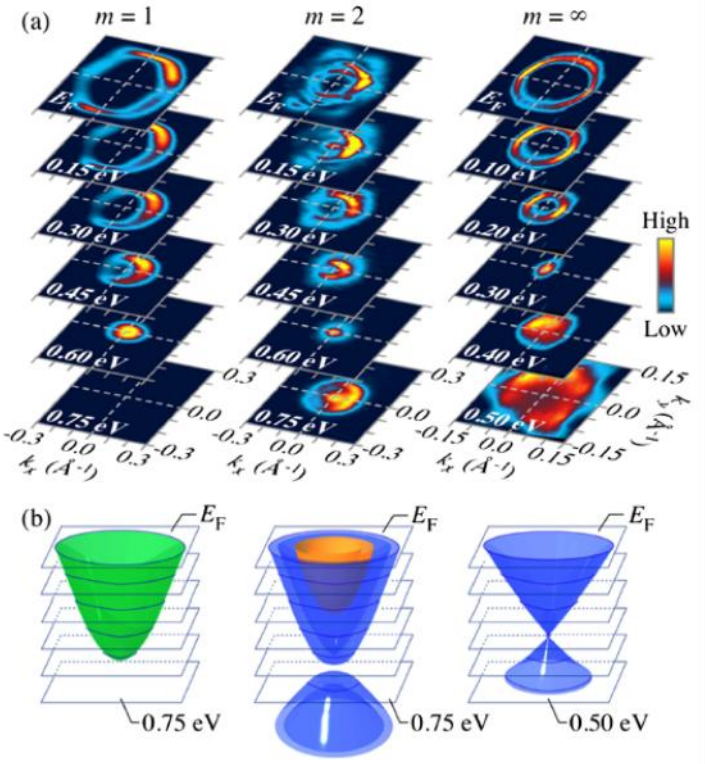

FIG. 5-6. (a)ARPES intensity mappings for m = 1, 2, and ∞ as a function of 2D wave vector at various E_B's. (b) Schematic 3D plots of the near-E_F band dispersions showing the energy positions at which the 2D intensity mappings in (a) are displayed.

Figure 5-7 summarizes the evolution of the near-E_F electronic structure upon varying m, highlighting the topological or nontopological nature of the phases. The hybridization gap in the Dirac-cone interface states observed for m = 2 is gradually reduced with increasing m, and it disappears at a characteristic m value, m_c, above which the coherent coupling between two adjacent interface states becomes negligibly weak. This change across m_c can be considered to be a nontopological to topological crossover. In contrast to the regular topological phase transition that accompanies a band inversion, this crossover is triggered by the 3D to 2D crossover of the system and the resultant loss of the characteristics of 3D topological insulators. It is also inferred that a band inversion takes place between m = 1 and 2, and this change is responsible for the observed marked difference in the band structure between the two. One can view such an evolution of electronic states as a consequence of the finite size effect in TI slabs embedded in naturally occurring heterostructures. Note that the critical thickness m_c is expected to be 6 QLs from the previous systematic ARPES and transport studies of Bi_2Se_3 ultrathin films [90,96]. Therefore, the fabrication of a system with $m \geq 6$ would be useful for realizing novel topological phenomena and TI-based applications which utilize the topologically protected interface states.

Perhaps more importantly, the present results bear significant implications on the band-gap engineering of TIs. Namely, as shown in Fig. 5-5, the magnitude of the bulk band gap for m = 2 is at least 0.5 eV, which is much larger than that for $m = \infty$ (~0.3 eV) [20] and is the largest ever observed in TIs. (Note that here what is appearing is the "bulk" band gap in the outermost Bi_2Se_3 unit; measurements of the inner Bi_2Se_3 units would require a bulk-sensitive experiment with hard x ray or low-energy photons.) This demonstrates that the bulk band gap can be enhanced by taking advantage of the quantization of the bulk bands in heterostructures.

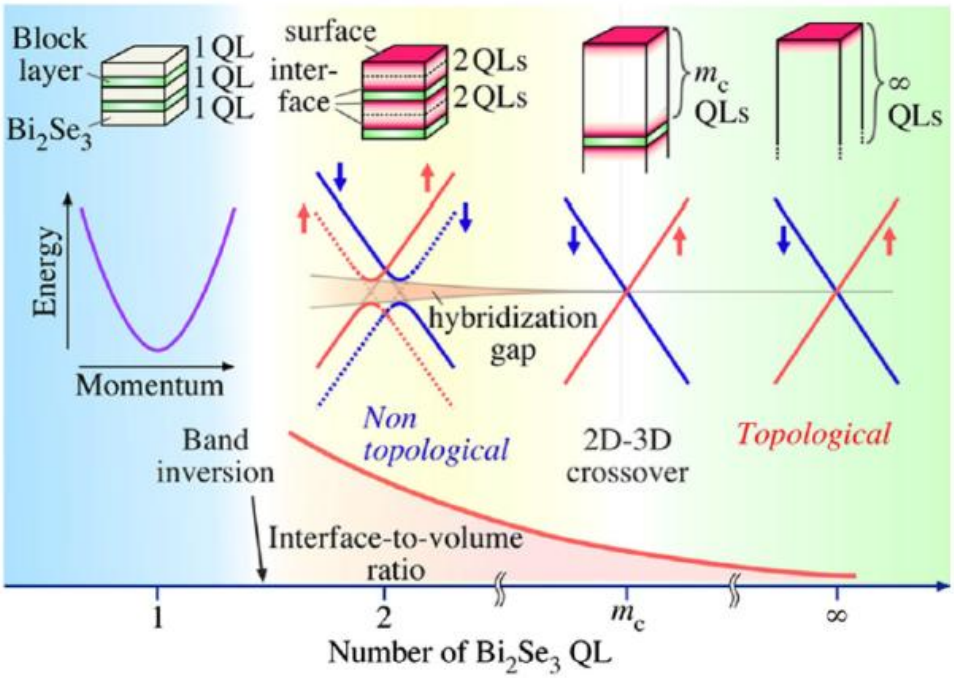

FIG. 5-7. Schematic band diagrams and illustrations of the heterostructures for various m values. Red area in heterostructures depicts the topological interface (surface) states. m_c is the characteristic thickness where the hybridization gap between two topological interface states starts to open. The interface-to-volume ratio is also shown schematically at the bottom.

It is useful to note that the existence of topological 2D states at the interfaces contained in naturally occurring heterostructures has a practical importance. It is well known that the surface of 3D TIs is prone to chemical reactions in ambient atmosphere [81,82,92], which has hampered transport studies of topological surface states that are prerequisite to device applications, calling for an efficient means to avoid surface degradation. Obviously, the topological interfaces found here reside in bulk crystals and hence are efficiently encapsulated from ambient atmosphere. Moreover, those interface states naturally lead to sizable interface-to-volume ratio (see Fig. 5-7), which would enhance their usability.

5.4 Conclusions

In conclusion, the present ARPES measurements of $(PbSe)_5(Bi_2Se_3)_{3m}$ revealed a Rashba splitting of topological 2D states for $m = 2$, providing the first experimental evidence for the existence of topological states at the heterostructure interface in the bulk. The natural multilayer structure leads to the capping of topological interface states and sizable interface-to-volume ratio. It was also found that the band dispersions of Bi_2Se_3 layers are quantized due to confinement effects and exhibit a drastic change upon varying m. In particular, the largest bulk band gap ever observed in TIs is achieved at $m = 2$. These results demonstrate that naturally occurring heterostructures are a promising playground for realizing novel topological phenomena and device applications of TIs.

Chapter 6 Summary

In this dissertation, experimental studies of topological insulators and related materials, with a focus on their transport properties, are described.

In Chapter 2, the study of the angular-dependent magnetoresistance in lead sulfide (PbS), which is one of the candidates for the spin Hall insulator, is described. The observed Shubnikov - de Haas oscillations show a spin splitting in the transverse measurement configuration, while in the longitudinal configuration, the amplitude of some peaks, in particular, 0^-, 1^+, and 2^+, are significantly diminished due to the selection rules, which are applied to systems with a strong spin orbit coupling. In addition, a peculiar angular-dependent magnetoresistance has been observed, although it is totally unexpected for a low-carrier-density PbS with nearly spherical Fermi surface. The origin of this unusual angular dependence of MR can be explained as an interplay between the spin-orbit coupling, the static skin effect, and the crossover between classical and quantum transport regimes in the magnetotransport of PbS. These results give a useful reference for studies of magnetotransport properties of narrow-gap semiconductors with a strong SOC, including TIs.

In Chapter 3, the study on the angular-dependent magnetoresistance in Bi_2Se_3, which is the most studied 3D topological insulator, is described. In a high-quality single crystal with the charge carrier concentration of 5×10^{18} cm^{-3}, pronounced angular-dependent oscillations of the MR together with clear Shubnikov-de Haas oscillations have been observed. The detailed simulation of the angular-dependent oscillations based on the information obtained from the SdH analysis led to the conclusion that the observed oscillations are due to the Landau quantization of the anisotropic 3D bulk Fermi surface, providing a useful tool for distinguishing 3D and 2D surface states in Bi_2Se_3 and other TIs.

In Chapter 4, the study on the Pb-based solid solution $Pb(Bi_{1-x}Sb_x)_2Te_4$ is described. It has been confirmed by ARPES experiments that this material is the first Pb-based topological insulator. In transport measurements, a sign change of charge carriers from *n*-type to *p*-type upon variation of Sb concentration was observed, although the bulk carrier density remained high even near the *n*- to *p*-type transition, reflecting the fact that major defects in $Pb(Bi_{1-x}Sb_x)_2Te_4$ are of substitutional and antisite nature.

In Chapter 5, the study on Pb-based homologous series $(PbSe)_5(Bi_2Se_3)_{3m}$ is described. It has been shown by ARPES measurements that the natural multilayer structure of $(PbSe)_5(Bi_2Se_3)_{3m}$ leads to the appearance of topological 2D states at the heterostructure interface in the bulk. It was clearly demonstrated that the band dispersions of Bi_2Se_3 layers are quantized due to confinement effects and exhibit a drastic change upon varying *m*. For $m = 1$ and $m = 2$, the observation of a single parabolic band and a pronounced Rashba splitting of topological 2D states, respectively, agrees perfectly well with the previous ARPES studies of Bi_2Se_3 ultra thin films [90]. The present results demonstrate that naturally occurring heterostructures can be promising for realizing novel topological phenomena and device applications.

References

[1] M. I. Dyakonov and V. I. Perel, Phys. Lett. A **35**, 459 (1971).

[2] S. Murakami, N. Nagaosa, and S.-C. Zhang, Science **301**, 1348 (2003) .

[3] J. Sinova, D. Culcer, Q. Niu, N. A. Sinitsyn, T. Jungwirth, and A. H. MacDonald, Phys. Rev. Lett. **92**, 126603 (2004).

[4] Y. K. Kato, R. C. Myers, A. C. Gossard, and D. D. Awschalom, Science **306**, 1910 (2004).

[5] E. Saitoh, M. Ueda, H. Miyajima, and G. Tatara, Appl. Phys. Lett. **88**, 182509 (2006).

[6] S. Murakami, N. Nagaosa and S.-C. Zhang, Phys. Rev. Lett. **93**, 156804 (2004).

[7] S. Murakami, S. Iso, Y. Avishai, M. Onoda, and N. Nagaosa, Phys. Rev. B **76**, 205304 (2007).

[8] C. L. Kane and E. J. Mele, Phys. Rev. Lett. **95**, 146802 (2005).

[9] C. L. Kane and E. J. Mele, Phys. Rev. Lett. **95**, 226801 (2005).

[10] L. Fu, C. L. Kane, and E. J. Mele, Phys. Rev. Lett. **98**, 106803 (2007).

[11] L. Fu and C. L. Kane, Phys. Rev. B **76**, 045302 (2007).

[12] B. A. Bernevig, T. L. Hughes, and S. C. Zhang, Science **314**, 1757 (2006).

[13] M. König, S. Wiedmann, C. Brüne, A. Roth, H. Buhmann, L. W. Molenkamp, X.-L. Qi, and S.-C. Zhang, Science **318**, 766 (2007).

[14] J. E. Moore and L. Balents, Phys. Rev. B **75**, 121306(R) (2007).

[15] R. Roy, Phys. Rev. B **79**, 195322 (2009).

[16] D. Hsieh, D. Qian, L. Wray, Y. Xia, Y. S. Hor, R. J. Cava, and M. Z. Hasan, Nature **452**, 970 (2008).

[17] D. Hsieh, Y. Xia, L. Wray, D. Qian, A. Pal, J. H. Dil, J. Osterwalder, F. Meier, G. Bihlmayer, C. L. Kane, Y. S. Hor, R. J. Cava, and M. Z. Hasan, Science **323**, 919 (2009).

[18] A. Nishide, A. A. Taskin, Y. Takeichi, T. Okuda, A. Kakizaki, T. Hirahara, K. Nakatsuji, F. Komori, Y. Ando, and I. Matsuda, Phys. Rev. B. **81**, 041309(R) (2010).

[19] H. Zhang, C.-X. Liu, X.-L. Qi, X. Dai, Z. Fang, and S.-C. Zhang, Nat. Phys. **5**, 438 (2009).

[20] Y. Xia, D. Qian, D. Hsieh, L. Wray, A. Pal, H. Lin, A. Bansil, D. Grauer, Y. S. Hor, R. J. Cava, and M. Z. Hasan, Nat. Phys. **5** 398 (2009).

[21] Y. L. Chen, J. G. Analytis, J.-H. Chu, Z. K. Liu, S.-K. Mo, X. L. Qi, H. J. Zhang, D. H. Lu, X. Dai, Z. Fang, S. C. Zhang, I. R. Fisher, Z. Hussain, and Z.-X. Shen, Science **325**, 178 (2009).

[22] D. Hsieh, Y. Xia, D. Qian, L. Wray, J. H. Dil, F. Meier, J. Osterwalder, L. Patthey, J. G. Checkelsky, N. P. Ong, A. V. Fedorov, H. Lin, A. Bansil, D. Grauer, Y. S. Hor, R. J. Cava, and M. Z. Hasan, Nature **460**, 1101 (2009).

[23] Z.-H. Pan, E. Vescovo, A.V. Fedorov, D. Gardner, Y. S. Lee, S. Chu, G. D. Gu, and T. Valla, Phys. Rev. Lett. **106**, 257004 (2011).

[24] S. Souma, K. Kosaka, T. Sato, M. Komatsu, A. Takayama, T. Takahashi, M. Kriener, K. Segawa, and Y. Ando, Phys. Rev. Lett. **106**, 216803 (2011).

[25] P. Roushan, J. Seo, C. V. Parker, Y. S. Hor, D. Hsieh, D. Qian, A. Richardella, M. Z. Hasan, R. J. Cava, and A. Yazdani, Nature **460**, 1106 (2009).

[26] T. Zhang, P. Cheng, X. Chen, J.-F. Jia, X. Ma, K. He, L. Wang, H. Zhang, X. Dai Z. Fang, X. Xie, and Q.-K. Xue, Phys. Rev. Lett. **103**, 266803 (2009).

[27] T. Hanaguri, K. Igarashi, M. Kawamura, H. Takagi, and T. Sasagawa, Phys. Rev. B **82**, 081305(R) (2010).

[28] H. Peng, K. Lai, D. Kong, S. Meister, Y. Chen, X.-L. Qi, S.-C. Zhang, Z.-X. Shen, and Y. Cui, Nat. Mater. **9**, 225 (2010).

[29] Y. S. Hor, A. Richadella, P. Roushan, Y. Xia, J. G. Checkelsky, A. Yazdani, M. Z. Hasan, N. P. Ong, and R. J. Cava, Phys. Rev. B **79**, 195208 (2009).

[30] J. G. Checkelsky, Y. S. Hor, M.-H. Liu, D.-X. Qu, R. J. Cava, and N. P. Omg, Phys. Rev. Lett. **103**, 246601 (2009).

[31] A. A. Taskin and Y. Ando, Phys. Rev. B **80**, 085303 (2009).

[32] A. A. Taskin, K. Segawa, and Y. Ando, Phys. Rev. B **82**, 121302(R) (2010).

[33] B. Yan and S.-C. Zhang, Rev. Prog. Phys. **75**, 096501 (2012).

[34] T. Sato, K. Segawa, H. Guo, K. Sugawara, S. Souma, T. Takahashi, and Y. Ando, Phys. Rev. Lett. **105**, 136802 (2010).

[35] K. Kuroda, M. Ye, A. Kimura, S. V. Eremeev, E. E. Krasovskii, E. V. Chulkov, Y. Ueda, K. Miyamoto, T. Okuda, K. Shimada, H. Namatame, and M. Taniguchi, Phys. Rev. Lett. **105**, 146801 (2010).

[36] Y. L. Chen, Z. K. Liu, J. G. Analytis, J.-H. Chu, H. J. Zhang, B. H. Yan, S.-K. Mo, R. G. Moore, D. H. Lu, I. R. Fisher, S. C. Zhang, Z. Hussain, and Z.-X. Shen, Phys. Rev. Lett. **105**, 266401 (2010).

[37] S.-Y. Xu, Y. Xia, L. A. Wray, S. Jia, F. Meier, J. H. Dil, J. Osterwalder, B. Slomski, A. Bansil, H. Lin, R. J. Cava, M. Z. Hasan, Science **332**, 560 (2011).

[38] T. Sato, K. Segawa, K. Kosaka, S. Souma, N. Nakayama, K. Eto, T. Minami, Y. Ando, and T. Takahashi, Nat. Phys. **7,** 840 (2011).

[39] C. Niu, Y. Dai, Y. Zhu, J. Lu, Y. Ma, and B. Huang, Appl. Phys. Lett. **101**, 182101 (2012).

[40] S. Souma, M. Komatsu, M. Nomura, T. Sato, A. Takayama, T. Takahashi, K. Eto, K. Segawa, and Y. Ando, Phys. Rev. Lett. **109**, 186804 (2012).

[41] J. Broem, Philips Res. Rep. **11**, 273 (1956).

[42] T. C. Harman and A. J. Strauss, J. Electron. Mater. **5**, 621 (1976).

[43] S. Abe and K. Masumoto, J. Cryst. Growth **249**, 544 (2003).

[44] R. Dalven, Infrared Phys. **9**, 141 (1969).

[45] P. J. Stiles, E. Burstein, and D. N. Langenberg, J. Appl. Phys.**32**, 2174 (1961).

[46] J. J. H. Pijpers, R. Ulbricht, K. J. Tielrooij, A. Osherov, Y. Golan,C. Delerue, G. Allan, and M. Bonn, Nat. Phys. **5**, 811 (2009).

[47] V. G. Peschanskii and M. Y. Azbel', Sov. Phys. JETP **28**, 1045 (1969).

[48] A. A. Abrikosov, J. Phys. A **36**, 9119 (2003).

[49] K. Suizu and S. Narita, Phys. Lett. A **43**, 353 (1973).

[50] S. Narita and Y. Takafuji, Solid State Commun. **20**, 357 (1976).

[51] D. Shoenberg, *Magnetic Oscillations in Metals* (Cambridge UniversityPress, Cambridge, 1984).

[52] S. Das Sarma and F. Stern, Phys. Rev. B **32**, 8442 (1985).

[53] Y. A. Bogod, V. V. Eremenko, and L. K. Chubova, Sov. Phys. JETP **29**, 17 (1969).

[54] Y. A. Bogod and V. B. Krasovitskii, Sov. Phys. JETP **36**, 544 (1973).

[55] G.R. Hyde, H. A. Beale, I. L. Spain, and J. A. Woollam, J. Phys. Chem. Solids **35**, 1719 (1974).

[56] J. G. Analytis, J.-H. Chu, Y. Chen, F. Corredor, R. D. McDonald, Z. X. Shen, and I. R. Fisher, Phys. Rev. B **81**, 205407 (2010).

[57] H. Köhler and A. Fabricius, Phys. Status Solidi (b) **71**, 487 (1975).

[58] H. Köhler and H. Fisher, Phys. Status Solidi B **69**, 349 (1975).
[59] M. V. Kartsovnik, P. A. Kononovich, N. V. Laukhin, and I. F. Shchegolev, JETP Lett. **48**, 541 (1988).
[60] K. Yamaji, J. Phys. Soc. Jpn. **58**, 1520 (1989).
[61] R. Yagi, Y. Iye, T. Osada, and S. Kagoshima, J. Phys. Soc. Jpn. **59**, 3069 (1990).
[62] G. M. Danner, W. Kang, and P. M. Chaikin, Phys. Rev. Lett. **72**, 3714 (1994).
[63] R. H. McKenzie and P. Moses, Phys. Rev. Lett. **81**, 4492 (1998).
[64] P. Moses and R. H. McKenzie, Phys. Rev. B **60**, 7998 (1999).
[65] B. K. Cooper and V. M. Yakovenko, Phys. Rev. Lett. **96**, 037001 (2006).
[66] R. N. Zitter, Phys. Rev. **127**, 1471 (1962).
[67] B. Yan, C.-X. Liu, H.-J. Zhang, C.-Y. Yam, X-L, Qi, T. Frauenheim, and, S.-C. Zhang, Europhys. Lett. **90**, 37002 (2010).
[68] H. Lin, R. S. Markiewicz, l. A. Waray, L. Fu, M. Z. Hasan, and A. Bansil, Phys. Rev. Lett. **105**, 036404 (2010).
[69] S. V. Eremeev, Y. M. Koroteev, and E. V. Chulkov, JETP Lett. **91**, 594 (2010).
[70] M. Neupane, S.-Y. Xu, L. A. Wray, A. Petersen, R. Shankar, N. Alidoust, C. Liu, A. Fedorov, H. Ji, J. M. Allred, Y. S. Hor, T.-R. Chang, H.-T. Jeng, H. Lin, A. Bansil, R. J. Cava, and M. Z. Hasan, Phys. Rev. B **85**, 235406 (2012).
[71] H. Jin, J. H. Song, A. J. Freeman, and M. G. Kanatzidis, Phys. Rev. B **83**, 041202(R) (2011).
[72] T.V. Menshchikova, S. V. Eremeev, Y. M. Koroteev, Y. M. Kuznetsov, and E. V. Chulkov, JETP Lett. **93**, 15 (2011).
[73] L. E. Shelimova, O. G. Karpinskii, P. P. Konstantinov, E. S.Avilov, M. A. Kretova, and V. S. Zemskov, Inorg. Mater. **40**, 451 (2004).
[74] L. E. Shelimova, T. E. Svechnikova, P. P. Konstantinov, O. G. Karpinskii, E. S. Avilov, M. A. Kretova, and V. S. Zemskov, Inorg. Mater. **43**, 125 (2007).
[75] L. E. Shelimova, O. G. Karpinskii, T. E. Svechnikova, M. A. Kretova, and V. S. Zemskov, Inorg. Mater. **40**, 1264 (2004).
[76] K. Kuroda, M. Arita, K. Miyamoto, M. Ye, J. Jiang, A. Kimura, E. E. Krasovskii, E. V. Chulkov, H. Iwasawa, T. Okuda, K. Shimada, Y. Ueda, H. Namatame, and M. Taniguchi, Phys. Rev. Lett. **105**, 076802 (2010).

[77] O.V. Yazyev, J. E. Moore, and S. G. Louie, Phys. Rev. Lett. **105**, 266806 (2010).

[78] L. E. Shelimova, O. G. Karpinskii, T. E. Svechnikova, I. Y. Nikhezina, E. S. Avilov, M. A. Kretova,and V. S. Zemskov, Inorg. Mater. **44**, 371 (2008).

[79] D. O. Scanlon, P. D. C. King, R. P. Singh, A. de la Torre, S. McKeown Walker, G. Balakrishnan, F. Baumberger, C. R. A. Catlow, Adv. Mater. **24**, 2154 (2012).

[80] D.-X. Qu, Y. S. Hor, J. Xiong, R. j. Cava, and N. P. Ong, Science **329**, 821 (2010).

[81] A. A. Taskin, Z. Ren, S. Sasaki, K. Segawa, and Y. Ando, Phys. Rev. Lett. **107**, 016801 (2011).

[82] D. Kong and Y. Cui, Nat. Chem. **3**, 845 (2011).

[83] M. G. Kanatzidis, Acc. Chem. Res. **38**, 359 (2005).

[84] Y. Zhang, A. P. Wilkinson, P. L. Lee, S. D. Shastri, D. Shu, D.-Y. Chung, and M. G. Kanatzidis, J. Appl. Crystallogr. **38**, 433 (2005).

[85] L. E. Shelimova, O. G. Karpinskii, and V. S. Zemskov, Inorg. Mater. **44**, 927 (2008).

[86] V. S. Zemskov, L. E. Shelimova, P. P. Konstantinov, E. S. Avilov, M. A. kretova, and I. Y. Nikhezina, Inorg. Mater. Appl. Res. **2**, 405 (2011).

[87] S. Souma, K. Eto, M. Nomura, K. Nakayama, T. Sato, T. Takahashi, K. Segawa, and Y. Ando, Phys. Rev. Lett. **108**, 116801 (2012).

[88] S. V. Eremeev, G. Landolt, T. V. Menshchikova, B. Slomski, Y. M. Koroteev, Z. S. Aliev, M. B. Babanly, J. Henk, A. Ernst, L. Patthey, A. Eich, A. A. Khajetoorians, J. Hagemeister, O. Pietzsch, J. Wiebe, R. Wiesendanger, P. M. Echenique, S. S. Tsirkin, I. R. Amiraslanov, J. H. Dil, and E. V. Chulkov, Nature Commun. **3**, 635 (2012).

[89] J. J. Yeh and I. Lindau, At. Data Nucl. Data Tables **32,** 1(1985).

[90] Y. Zhang, K. He, C.-Z. Chang, C.-L. Song, L.-L. Wang, X. Chen, J.-F. Jia, Z. Fang, X. Dai, W.-Y. Shan, S.-Q. Shen, Q. Niu, X.-L. Qi, S.-C. Zhang, X.-C. Ma, and Q.-K. Xue, Nat. Phys. **6**, 584 (2010).

[91] P. D. C. King, R. C. Hatch, M. Bianchi, R. Ovsyannikov, C. Lupulescu, G. Landolt, B. Slomski, J. H. Dil, D. Guan, J. L. Mi, E. D. L. Rienks, J. Fink, A. Lindblad, S. Svensson, S. Bao, G. Balakrishnan, B. B. Iversen, J. Osterwalder, W. Eberhardt, F. Baumberger, and Ph. Hofmann, Phys. Rev. Lett. **107**, 096802 (2011).

[92] H. M. Benia, C. Lin, K. Kern, and C. R. Ast, Phys. Rev. Lett. **107**, 177602 (2011).
[93] C.-X. Liu, H. J. Zhang, B. Yan, X.-L. Qi, T. Frauenheim, X. Dai, Z. Fang, and S.-C. Zhang, Phys. Rev. B **81**, 041307(R) (2010).
[94] H.-Z. Lu, W.Y. Shan, W. Yao, Q. Niu, and S. Q. Shen, Phys. Rev. B **81**, 115407 (2010).
[95] Y. Sakamoto, T. Hirahara, H. Miyazaki, S. I. Kimura, and S. Hasegawa, Phys. Rev. B **81**, 165432 (2010).
[96] A. A. Taskin, S. Sasaki, K. Segawa, and Y. Ando, Phys. Rev. Lett. **109**, 066803 (2012).

List of Publications

1. Spin-orbit coupling and anomalous angular-dependent magnetoresistance in the quantum transport regime of PbS
   Kazuma Eto, A. A. Taskin, Kouji Segawa, and Yoichi Ando
   Physical Review B **81**, 161202-1－161202-4 (2010).

2. Angular-dependent oscillations of the magnetoresistance in Bi_2Se_3 due to the three-dimensional bulk Fermi surface
   Kazuma Eto, Zhi Ren, A. A. Taskin, Kouji Segawa, and Yoichi Ando
   Physical Review B **81**, 195309-1－195309-5 (2010).

3. Topological Surface States in Lead-Based Ternary Telluride $Pb(Bi_{1-x}Sb_x)_2Te_4$
   S. Souma, K. Eto, M. Nomura, K. Nakayama, T. Sato, T. Takahashi, Kouji Segawa, Yoichi Ando
   Physical Review Letters **108**, 116801-1－116801-5 (2012).

4. Manipulation of Topological States and the Bulk Band Gap Using Natural Heterostructures of a Topological Insulator
   K. Nakayama, K. Eto, Y. Tanaka, T. Sato, S.Souma, T. Takahashi, Kouji Segawa, and Yoichi Ando
   Physical Review Letters **109**, 236804-1－236804-5 (2012).

5. Transport properties of Pb-based topological insulator $Pb(Bi_{1-x}Sb_x)_2Te_4$ solid-solution system
   Kazuma Eto, Satoshi Sasaki, Kouji Segawa, and Yoichi Ando
   Journal of the Physical Society of Japan, *submitted*.

Supplementary Publications

1. Unexpected mass acquisition of Dirac fermions at the quantum phase transition of a topological insulator
   T. Sato, Kouji Segawa, K. Kosaka, S. Souma, K. Nakayama, K. Eto, T. Minami, Yoichi Ando, and T. Takahashi
   Nature Physics **7**, 840-844 (2011).

2. Spin Polarization of Gapped Dirac Surface States Near the Topological Phase Transitionin $TlBi(S_{1-x}Se_x)_2$
   S. Souma, M. Komatsu, M. Nomura, T. Sato, A. Takayama, T. Takahashi, K. Eto, Kouji Segawa, and Yoichi Ando
   Physical Review Letters **109**, 186804-1－186804-5 (2012).

Acknowledgements

I would like to express my gratitude to Professor Dr. Yoichi Ando of the Institute of Scientific and Industrial Research, Osaka University, for his continuous guidance, helpful suggestions, and fruitful discussions throughout this work. I would also like to thank Professor Dr. Nobuhito Imanaka and Professor Dr. Susumu Kuwabata of the Division of Applied Chemistry for reviewing this thesis and their helpful advices.

I am deeply grateful to Prof. Kouji Segawa, Prof. Alexey Taskin, and Prof. Satoshi Sasaki for their useful advices, help and encouragement.

I am obliged to Prof. Seigo Souma, Prof. Nakayama Kosuke, and Prof. Takafumi Sato, Tohoku University, for ARPES measurements.

I appreciate my colleagues, Dr. Zhi Ren, Dr. Markus Kriener, Dr. Mario Novak, Dr. Fan Yang, Daisuke Hama, Tatsuya Minami, Ryouhei Yoshida, Syohei Wada, Takumi Ueyama, Kazuto Kinoshita, Toshinobu Toba, and Megumi Kishi, for their helpful assistance and support in the course of this work. I also thank to Mr. Hiromi Makiyama, Prof. Takafumi Kusunose, and Prof. Sekino Tohru for their support and hearty encouragement.

The Japan Society for the Promotion of Science is also acknowledged for a research fellowship.

Finally, I would like to deeply thank my parents Shoichi Eto and Kayoko Eto, my brother Yuki Eto, my sister Rina Eto, and all members of my family for their generous understanding and support.

Kazuma Eto
January, 2013